

https://dspace.org/

Computed tomography image processing and reconstruction using the ASTRA toolbox

Chinamatira, Gideon

2022

https://hdl.handle.net/10539/34569

Downloaded from a DSpace repository. https://dspace.org/

Computed tomography image processing and reconstruction using the ASTRA toolbox

Gideon Chinamatira

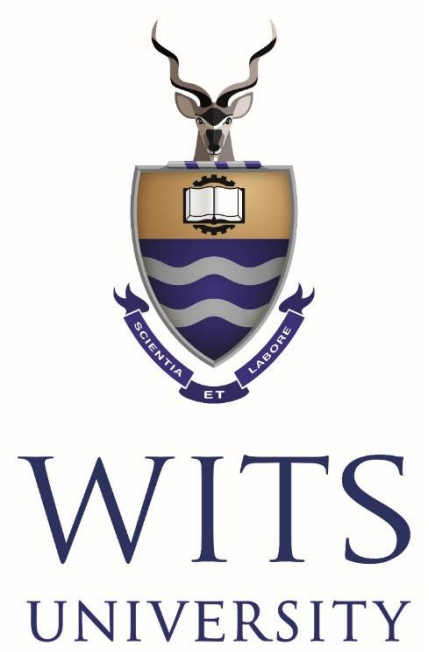

A dissertation submitted to the Faculty of Science, University of the Witwatersrand Johannesburg in the fulfillment of the academic requirements for the degree of Master of Science.

June 03 , 2022

Declaration

I, **Gideon Chinamatira,** declare that this thesis is my own original work and that it has not been presented and will not be presented to any other institution for a similar or any other degree award**.**



(Signature of the candidate)

June 03, 2022

Dedication

In loving memory of Andrea Leenen (1972-2022). May her soul continue to rest in peace.

Acknowledgements

I would like to thank God for the guidance and blessing to complete this research work. I would also like to thank my supervisors Dr. K. Jakata and Dr. B. Mathe for their commitment and guidance throughout the entire project life span. My extended gratitude goes to the Palaeontological Scientific Trust for the financial support throughout the studies as well as the Evolutionary Studies Institute at the University of the Witwatersrand for allowing me to use the equipment necessary to complete the research work. Last but not least, I would like to thank my family and friends for the encouragement and support which gave me the passion and extra drive to see off this research work unto completion.

Abstract

The computed tomography (CT) technique has become pivotal to research in fields such as palaeontology, health studies, engineering, and materials science. This imaging technique makes use of x-ray absorption in order to obtain three-dimensional (3D) images. However, imaging can be challenging when objects of high-density materials are included in the matrix with lower-density material. Extremely bright regions, streaks, and scattering can result in such cases thereby reducing contrast and also making the data less usable. There are several algorithms that are used at the stage of image reconstruction when the 3D volume is generated from radiographic projections such as the filtered back projection (FBP). Backprojection has two distinctive limitations, noise, and streak artefacts and it is a combination of these restrictions and the advancement of computers that iterative algorithms are seen as the possible candidate to replace this method of image reconstruction to subsequently reduce these artefacts.

We report an investigation on the effects of adding an image processing step before performing computed tomography reconstructions. We have acquired projections with a micro-computed tomography scanner and carried out image processing functions for the improvement of the quality of the data output using a paleontological specimen with a significant amount of iron inclusions which cause bright and dark streak artefacts. We have applied several filters to alter the projections before reconstruction. The results so far show that the minimum filter, median and the mean filter reduces the noise and streak artefacts in the specimen. The Gaussian smoothing filter also successfully reduces the noise in the images, but the streak artefacts are still significantly visible. The unsharp mask filter enhances the edges in the images and reduces the streak artefacts significantly. However, this filter enhances other high-frequency components in an image causing an increase in the noise.

In this project, we have also used the ASTRA toolbox in order to implement iterative algorithms for 3D reconstruction. This will give us an alternative to the proprietary software that makes use of the FBP algorithm. This will also give use additional capabilities such as customizing the reconstruction process and developing phase retrieval reconstruction methods that can be used to enhance contrast. The ASTRA toolbox uses graphics processing units (GPUs) to allow for parallel processing of CT data and thereby reducing the reconstruction time. We will demonstrate reconstructions with up to 300 projections of a few samples using the simultaneous iterative reconstruction technique (SIRT).

Table of Contents

Declaration i

Dedication ii

Acknowledgements iii

Abstract iv

List of figures viii

Chapter 1: Introduction 1

1.1 Introduction 1

1.2 Image reconstruction 2

1.2.1 The Radon Transform 2

1.2.2. The Fourier slice theorem 3

1.3 Iterative reconstruction techniques 4

1.4 The rationale for this research 5

1.5 Aim 5

1.6 Hypothesis and Questions 6

1.7 Dissertation organisation 6

References: Chapter 1 7

Chapter 2: Fundamentals of x-ray physics 8

2.1 Introduction 8

2.2 X-ray generation 8

2.3 Beam filtering 11

2.4 Interaction of x-rays with matter 12

2.5 X-ray detection 17

2.5.1 Gas detectors 17

2.5.2 Solid-state scintillator detector 18

2.5.3 Solid-State Flat-Panel Detectors 20

2.5.4 Properties of XCT detectors 21

References: Chapter 2 23

Chapter 3: Image reconstruction 25

3.1 Introduction 25

3.2 Parallel beam tomography 25

3.3 Fan beam geometry 26

3.4 Cone-beam geometry 27

3.5 Computed tomography kinematic systems 28

3.6 Software 29

3.7 The problem of image reconstruction: CT artefacts 29
3.7.1 Metal artefacts 29
3.7.2 Scatter radiation and beam hardening artefacts 30
3.7.3 Noise 31
3.7.4 Ring artefacts 32
3.8 Algebraic reconstruction methods 33
3.8.1 Simultaneous iterative reconstruction technique (SIRT) 34
3.9 Graphics Processing Units 35
3.10 The ASTRA toolbox 37
3.10.1 Projection and volume data 38
3.10.2 Geometry 38
3.10.3 Reconstruction algorithms 40
3.11 Application of the ASTRA toolbox to experimental setups 41
3.12 Sinograms 43
References: Chapter 3 45
4 Pre-processing of projection data 46
4.1 Introduction 46
4.2 Convolution Filtering 46
4.3 Experimental procedure 47
4.3.1 Mean Filter 48
4.3.2 Median Filter 49
4.3.3 Gaussian smoothing 50
4.3.4 Unsharp filter 51
4.4 A quantitative approach to image quality evaluation 53
4.4.1 Image quality 54
4.4.2 Standard deviation 54
4.4.3 Image noise 54
4.5 Image quality results 57
4.5.1 No filter 58
4.5.3 Mean filter 59
4.5.4 Median Filter 59
4.5.5 Unsharp mask filter 59
4.6 Conclusions 60
References: Chapter 4 61
5 Reconstruction with the ASTRA toolbox 63
5.1 Introduction 63

5.2 Flat field correction with the ASTRA toolbox 63
5.2.1 Normalization 63
5.2.2 Dark current 63
5.2.3 Flatfields 64
5.3 Correction of center of rotation (COR) misalignments 65
5.4 Conventional cone-beam reconstruction 67
Chapter 6: Discussion and Conclusion 75
6.1 Introduction 75
6.2 Image processing before reconstruction 75
6.3 SIRT reconstruction with the ASTRA toolbox 76
6.4 Future work 77

List of figures

Figure 1.1: Schematic of the X-ray computed tomography technique. 1

Figure 1.2 : Tomographic reconstruction. Each projection, resulting from tomography under a specific angle, is made up of the set of line integrals through the object. 3

Figure 2.1:Schematic of an x-ray tube structure [2]. 9

Figure 2.2: Sketch of the process involved in x-ray generation. (a) Bremsstrahlung and (b) characteristic radiation. 10

Figure 2.3**:** Bremsstrahlung and characteristic radiation spectra are shown for a tungsten anode with x-ray tube operation at 100 kV. 10

Figure 2.4: Beam hardening of an X-ray spectrum produced by a tungsten anode due to filtering by a 2 mm copper filter. 12

Figure 2.5: Photoelectric absorption 12

Figure 2.6: Compton scattering process 13

Figure 2.7: principles of photon–matter interaction via the Rayleigh scattering 15

Figure 2.8: Principles of photon–matter interaction via the pair production 16

Figure 2.9: Mass attenuation coefficient, μ/ρ, versus incident photon energy for Pb [14]. 16

Figure 2.10: Schematic cut-out of two adjacent ionizing chambers of a xenon high-pressure detector array. Since the chambers are communicating, all detector elements have the same Xe pressure and, therefore, the same sensitivity. 18

Fig 2.11. Mass attenuation coefficient for the main photon–matter interaction principles in detector materials. Photoelectric absorption is more than one magnitude higher than scattering processes in xenon and the Gd_2O_2S ceramic [14]. 19

Figure 2.12: Schematic of a scintillator x-ray detector 19

Fig 2.12**:** Schematic of a digital flat-panel X-ray detector. 20

Figure 3.1: A schematic of parallel beam tomography. 25

Figure 3.2: Simplified representation of a fan beam scanning scenario 26

Figure 3.3: Schematic of the x-ray computed tomography technique showing a flat panel detector 27
Figure 3.4: Three samples arranged in line with the direction of the x-ray beam towards the detector. 28
Figure 3.5: A cross-section of an image 3D rendering after reconstructing tomographic projections of a palaeontological specimen with metallic inclusions. 30
Figure 3.6: A cross-section of 3D rendering from a CT scan of a skull of the fossil primate *Rooneyia viejaensis* showing beam hardening effects. 31
Figure 3.7: A cross-section of a 3D rendering from tomographic projections of a dinosaur coprolite showing the noise which is observed from how grainy the image is. 32
Figure 3.8: Ring artefacts from a cross-section of 3D rendered data of a sample after reconstructing from 2D projections. 33
Figure 3.9. Schematic overview of the ASTRA Toolbox design. 37
Fig 3.10: Showing the Astra toolbox modules and how they are connected [12]. 38
Figure 3.11: Approach to the specification of vector-based cone-beam projection geometry.41
Figure 3.12: An auxiliary illustration for vector-based image reconstruction. 43
Figure 3.13: A sinogram from CT data 44
Figure 4.1: Tooth of an *anteosaurcus magnificus* used as the test specimen. 47
Figure 4.2: A cross-sectional view of the tooth of an *anteosaurcus magnificus*. 48
Figure 4.3: Shows a cross-sectional view of the specimen after applying a mean filter of radius 1 pixel (a) and 2 pixels(b) 49
Figure 4.4**:** Shows a cross-sectional view of the specimen after applying a median filter of radius1 pixel (a) and 2 pixels (b). 50
Figure 4.5: Shows a cross-sectional view of the specimen after applying a gaussian filter of sigma radius 1(a) and 2 (b). 51
Figure 4.6: Shows a cross-sectional view of the specimen after applying an unsharp mask filter of sigma radius 1 pixel (a) and 2 pixels (b) with a mask weight of 0.60. 52
Figure 4.7: Histogram showing the grey values of the tooth of an *anteosaurcus magnificus* obtained from CT and then reconstruction using CT Pro 3D. 53

Figure 4.8: Full width at half maximum for the *anteosaurcus magnificus* when no filter was applied. 55
Figure 4. 9: Region of interest to measure the background noise in the image. 57
Figure 4.10: The effect of varying filtering options on the image quality. 57
Figure 4.11: Background noise measured as the FWHM. 58

Figure 5.1: An ideal cone-beam scanning experimental setup 64

Figure 5.2: COR shift caused by horizontal displacement of the rotational axis from the optical axis. 65

Figure 5.3: (a) A cross-sectional view of the reconstruction of the tooth with the SIRT algorithm in the ASTRA toolbox using 300 projections, (b) A cross-sectional view of the reconstruction of the same specimen with the FBP algorithm in CT Pro 3D using 300 projections, and (c) A cross-sectional view of the reconstruction of the same specimen with the FBP algorithm in CT Pro 3D using 3000 projections. 69

Figure 5.4: (a) A cross-sectional view of the reconstruction of the proximal femur with the SIRT algorithm in the ASTRA toolbox using 300 projections, (b) A cross-sectional view of the reconstruction of the same specimen with the FBP algorithm in CT Pro 3D using 300 projections, and (c) A cross-sectional view of the reconstruction of the same specimen with the FBP algorithm in CT Pro 3D using 3000 projections. 70

Figure 5.5: A grey value distribution analysis for the tooth reconstructed when reconstructed with the ASTRA toolbox using 300 projections. 71
Figure 5.6: A grey value distribution analysis for the tooth reconstructed when reconstructed with CT Pro 3D toolbox using 3000 projections. 71
Figure 5.7: A grey value distribution analysis for the tooth reconstructed when reconstructed with the ASTRA toolbox using 300 projections. 72

Figure 5.8: A grey value distribution analysis for the tooth reconstructed when reconstructed with CT Pro 3D using 3000 projections. 72

Chapter 1: Introduction

1.1 Introduction

There has been a persistent drive towards the improvement of image quality obtained for research, industrial and clinical applications since the first computed tomography scan in the early 1970s [1]. The computed tomography (CT) technique is a non-invasive imaging method that is used to generate 3-dimensional (3D) images from a series of 2-dimensional (2D) x-ray projections. The technique has seen extensive use because of its ability to create accurate virtual representations of both the external and the internal features of a specimen. The cone-beam computed tomography (CBCT) setup shown in figure 1.1 has an x-ray source, detector, and a rotating sample stage. The 2D X-ray projections used to reconstruct the 3D images are collected through a full 360 degrees rotation of the specimen [2]. CT is based on the principle that the density of an object traversed by an x-ray beam can be measured from calculations of the attenuation coefficient of the absorbing material. The image quality of CBCT can be degraded by the presence of metal artefacts in the scanned volume [2]. When an image is reconstructed using CT data with these metal artefacts, it leads to changes in appearance that can be observed as dark or bright streaks thereby reducing contrast and also making the data less usable [2]. Since the artefacts result in loss of information, various methods have been developed for their reduction in a bid to improve the quality of the CT data obtained [3].

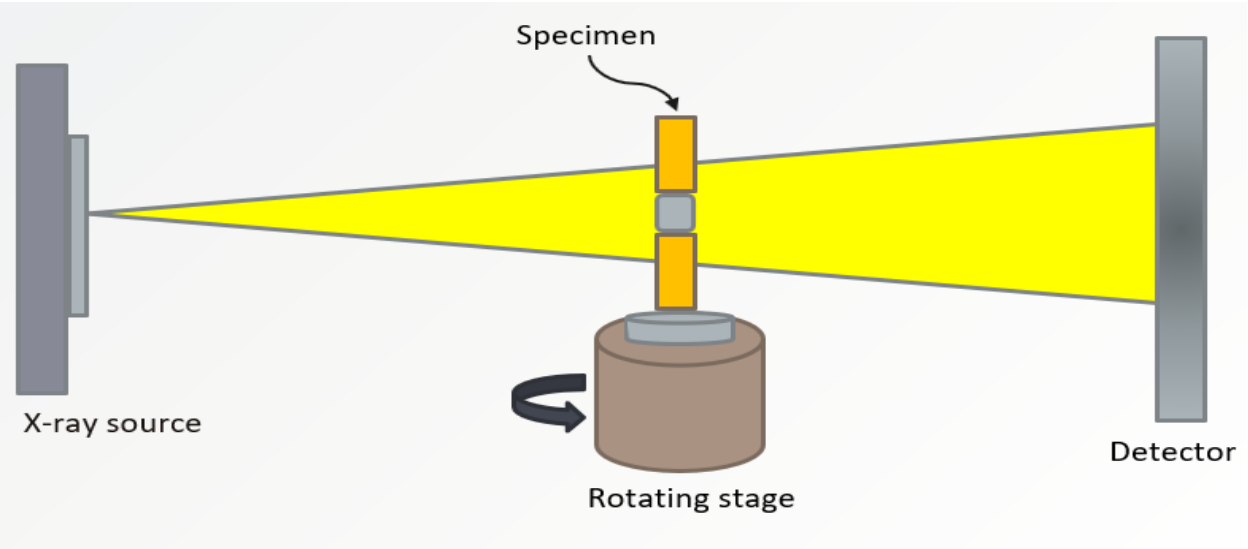

Figure 1.1: Schematic of the x-ray computed tomography technique.

1.2 Image reconstruction

There is a reduction in intensity when an x-ray beam travels through an object. The attenuation occurs according to the Beer Lambert law:

$$I = I_0 e^{(-\int \mu(x,y)ds)}, \tag{1.1}$$

where I is the x-ray intensity that reaches the detector, I_0 is the initial intensity emanating from the x-ray source, $\mu(x,y)$ is the attenuation coefficient as a function of position, therefore, the total attenuation ρ of an x-ray beam at position *r* on the projection at any given angle θ is given by the line integral

$$\rho_\theta(r) = \ln\left(\frac{I}{I_0}\right) = \int \mu(x,y)ds. \tag{1.2}$$

Although image reconstruction is a very computationally intensive process, it is a very crucial step in CT imaging. During data acquisition, the individual pixels on the detector represent the line integral of the sum of x-ray attenuation coefficients along the projection line. An attenuation coefficient is a measure of the quantity of radiation absorbed or scattered by a given thickness of the absorber [3]. There are a number of parallel paths through the object which define a sectional plane or a CT slice. On the other hand, there is also an inhomogeneous attenuation of the x-rays along the integration length. It is as advantageous to use the Radon transform and define the projection integral as a function of the linear position of the x-ray source, the projection angle, and the corresponding detector element.

1.2.1 The Radon Transform

Figure 1.2 below shows a 2D object on a cartesian coordinate system defined by a function *f (x, y).* Using the coordinate system in figure 2, the value of *r* for which the point *(x, y)* will be projected at an angle θ is given by

$$x\cos\theta + y\sin\theta = r, \tag{1.3}$$

so we can rewrite equation 1.2 as

$$\rho_\theta(r) = \int_{-\infty}^{\infty}\int_{-\infty}^{\infty} f(x,y)\sigma(x\cos\theta + y\sin\theta - r)dxdy. \tag{1.4}$$

This function is known as the Radon transform of the object [4]**,** where *(δ)* is the Dirac delta function that selects the line $x\cos\theta + y\sin\theta - r$ which connects the x-ray source and the

detector at r whilst rotating through an angle θ. This process is used to turn function values $f(x, y)$ into line integrals $\rho(r, \theta)$ whose values are recorded at the detector.

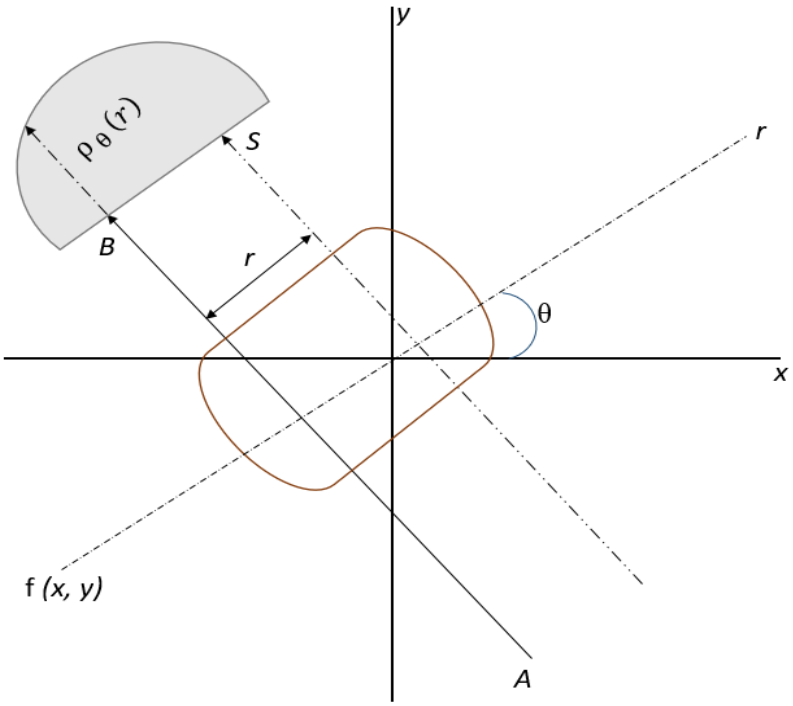

Figure 1.2: Tomographic reconstruction. Each projection, resulting from tomography under a specific angle, is made up of the set of line integrals through the object.

Given a function f representing an unknown density, the Radon transform represents the projection data which is obtained as the output of a CT scan. The inverse Radon transform derived from the Fourier slice theorem can then be used to reconstruct the original density from the projection data.

1.2.2. The Fourier slice theorem

According to the Fourier slice theorem, the one-dimensional Fourier transform $P(\omega, \theta)$ of a set of projections $P(r, \theta)$ for a fixed rotation angle θ is the same as the one-dimensional profile through the origin of the 2D Fourier transform $F(\omega \cos\theta, \omega \sin\theta)$ of the specimen $f(x, y)$ [5]. The transform of the projection can be written as

$$P(\omega, \theta) = \int_{-\infty}^{\infty} \int_{-\infty}^{\infty} f(x, y)\ e^{-j\omega(x \cos\theta + y \sin\theta)} dx dy, \qquad (1.5)$$

and can be used to represent an image in its cosine and sine components. This transform converts an input image in the spatial domain to produce a representation of an image in the

equivalent frequency domain [5]. For a given angle θ, $P(\omega, \theta)$ is a representation of a section of the 2D Fourier transform *f (x, y).*

The formula of the inverse radon transform can be derived from the inverse of the Fourier transform as

$$f\ (x,y) = \frac{1}{2\pi}\int_0^{\pi} g_{\theta}\ (x\cos\theta\ +\ y\sin\theta\ ), \tag{1.6}$$

where $g_{\theta}\ (x\ cos\ \theta\ +\ y\ sin\ \theta\ )$ is derived from the Hilbert transform of $\rho_{\theta}\ (r)$. The inverse Radon transform yields the original image. According to the Fourier slice theorem, the object *f (x, y)* can be reconstructed from an infinite number of 1- dimensional projections taken at an infinite number of angles.

The filtered back projection (FBP) algorithm has been widely favored for CT reconstruction due to its lower computational cost. In a back-projection process, the x-ray path is divided into evenly separate elements with each of these elements presumed to have contributed equally to the total x-ray attenuation. A total attenuation coefficient of the specimen can then be obtained by adding up the attenuation for each element at different angular orientations. The phenomenon results in a blurred image of the actual specimen when the simple back projection is used [5]. A filtering step is therefore added to correct this blurring, in a process known as filtered back projection. When FBP is used, artefacts can be reduced by applying corrections before generating the 3D data or in the postprocessing stage. Beam hardening and scatter are compensated for by subtracting their estimated effect from the raw data whilst noise is reduced by applying a low-pass filter to the raw data. In the presence of high-density inclusions such as metals, the effects of noise, scattered radiation, and beam hardening cause the FBP algorithm to produce reconstructions that are characterized by streaking artefacts, and there is room for implementing alternative reconstruction algorithm and developing more metal artefact reduction techniques.

1.3 Iterative reconstruction techniques

Iterative reconstruction algorithms provide an alternative to the FBP. These successive approximation methods were used to obtain an image of attenuation coefficients from the measured intensities. The process compares the data obtained from a CT scan to an assumed output and makes corrections to bring the two into an agreement. The process is repeated until the CT data is within acceptable limits or the same as the expected output. Iterative reconstruction methods come in three variations [6]. First is the simultaneous reconstruction in

which all projections are calculated at the beginning of the iteration, and all corrections for each iteration are made simultaneously. Secondly, the ray-by-ray correction by which only one ray sum is calculated and corrected, and future ray sums will be corrected using the first ray sum as a reference. Lastly, the point-by-point correction in which calculations and corrections are made for all rays passing through a point will be used in future calculations, and the process repeated for every point.

1.4 The rationale for this research

In this project, we are implementing alternative reconstruction techniques for computed tomography data. We have the capability of reconstructing using the FBP algorithm encoded in the proprietary software acquired with our Nikon XTH 250 instrument. However, this does not give us the capability to customize, use alternative algorithms and add additional features such as phase retrieval and image stitching among others.

Additionally, in the follow-up project, we want to be able to use these alternative algorithms to find ways to reduce the effects of high-density inclusions based on the CT scanning of fossils which can be preserved with metallic nodules. The location and orientation of these artefacts are not static but correlated to the rotation axis of the associated CT scan and we will use this fact together with the iterative reconstruction algorithms to minimize the high-density artefacts.

There are benefits of implementing alternative algorithms to improve the reconstruction process and subsequently the image quality obtained. The ASTRA toolbox provides a flexible and efficient set of tools for CT reconstruction. Due to its scalability, reconstruction methods and their parameters can be evaluated on small-size datasets such as CT simulations [8]. Afterwards, the resulting reconstruction strategy can then be deployed on large-scale datasets.

1.5 Aim

The aim of this research project is to improve the quality of data obtained from computed tomography experiments on samples with high-density inclusions:

- Make use of the ASTRA toolbox to investigate 3D data reconstruction algorithms from the projection images.
- Implementation of image processing software's such as ImageJ to carry out standard image processing functions that can be used to improve CT data.

- Reduce the effects of high-density inclusions in the 3D data obtained from CT scanning of rocks.

1.6 Hypothesis and Questions

The CT scanning of fossils is associated with the loss of contrast and streaking artefacts which are observed in the data obtained from a specimen with high-density inclusions. This causes the loss of valuable detail necessary for image reconstruction and segmentation. The above-mentioned constraints draw the need to improve the available as well as develop image reconstruction techniques with the goal to improve the quality of the CT scan data obtained from fossils.

One of the major problems of iterative methods is the increased computational effort and time which is required to perform multiple iterations. In this work, we want to investigate the effect of the implementation GPU based algorithms in CBCT in terms of reconstruction time and image quality.

1.7 Dissertation organisation

The first chapter of this report provides a brief description of our current understanding of computed tomography (CT) reconstruction algorithms and the need for the reduction of the effects of metallic inclusions. Further, the chapter describes the aim, research objectives, as well as research hypothesis. Chapter 2 gives an account of the fundamentals of x-ray physics with a particular focus on the production of x-rays as well as the interaction of x-rays with matter. It also provides an insight into x-ray detection and the properties of x-ray detectors. Chapter 3 discusses image reconstruction in CT, with particular attention to 3D image reconstruction algorithms (The FBP and iterative reconstruction algorithms). It also gives a review of the ASTRA toolbox for the implementation of iterative reconstruction algorithms. Chapter 4 focuses on image processing techniques such as the use of ImageJ to alter CT data by the use of various filters and tools provided by the software. Chapter 5 describes the approach used to gather the information and perform CT data reconstruction using the ASTRA toolbox, as well the results obtained. Chapter 6 gives a summary of the research process, clearly formulating the findings and conclusions regarding the research problem and hypothesis.

References: Chapter 1

1. Hounsfield, G.N., 1973. Computerized transverse axial scanning (tomography): Part 1. Description of system. *The British journal of radiology*, *46*(552), pp.1016-1022.
2. Warnett, J.M., Titarenko, V., Kiraci, E., Attridge, A., Lionheart, W.R., Withers, P.J. and Williams, M.A., 2016. Towards in-process x-ray CT for dimensional metrology. *Measurement Science and Technology*, *27*(3), p.035401.
3. Abdoli, M., Mehranian, A., Ailianou, A., Becker, M. and Zaidi, H., 2016. Assessment of metal artifact reduction methods in pelvic CT. *Medical physics*, *43*(4), pp.1588-1597.
4. Radon, J., 1986. On the determination of functions from their integral values along certain manifolds. *IEEE transactions on medical imaging*, *5*(4), pp.170-176.
5. Hsieh, J., Nett, B., Yu, Z., Sauer, K., Thibault, J.B. and Bouman, C.A., 2013. Recent advances in CT image reconstruction. *Current Radiology Reports*, *1*(1), pp.39-51.
6. Guhathakurta, J., Kiess, S., Hillebrand, J., Denecke, J., Effenberger, I. and Simon, S., 2015. Reducing Computed Tomography Reconstruction and Beam Hardening Artefacts by Data Fusion. In *International Symposium on Digital Industrial Radiology and Computed Tomography (DIR)* (pp. 330-337).
7. Ballhausen, H., Reiner, M., Ganswindt, U., Belka, C. and Söhn, M., 2014. Post-processing sets of tilted CT volumes as a method for metal artifact reduction. *Radiation Oncology*, *9*(1), pp.1-10.
8. Palenstijn, W.J., Bédorf, J. and Batenburg, K.J., 2015. A distributed SIRT implementation for the ASTRA toolbox. *Proc. Fully Three-Dimensional Image Reconstruct. Radiol. Nucl. Med*, pp.166-169.

Chapter 2: Fundamentals of x-ray physics

2.1 Introduction

X-rays are a highly penetrating form of electromagnetic radiation which were discovered in 1895 by German scientist Wilhelm Conrad Rontgen [1]. R*ö*entgen further discovered the imaging use of x-rays when he took a picture of his wife's hand which was formed on a photographic plate [1]. He immediately sent letters to the physicians that he knew around Europe explaining his discovery. The use of x-rays was extended to clinical conditions in January 1896 when John Hall-Edwards radiographed a needle that was stuck in one of his co-worker's hands [2]. R*ö*entgen continued with his experiments and came up with a method for live x-ray image viewing using a luminescent screen. Soon after R*ö*entgen's discovery, Thomas Edison an American inventor started research on material's ability to fluoresce when exposed to x-rays. In his work, he found out that calcium tungstate was the most effective substance. In 1896, he developed the fluoroscope which became the standard of x-ray examinations. By the 1930s tomography had been developed for cross-sectional imaging. In the 1970s, Cormack developed a theoretical underpinning of CT scanning and a 3D extension of the 2D x-ray technology, called computed tomography (CT), which was invented in 1972 by Godfrey Hounsfield [3]. This technique has found widespread applications in fields such as medical diagnostics, palaeontology, geology, anatomical sciences, and materials science. There has been a persistent drive to improve this CT technology to achieve faster image reconstruction, a higher spatial resolution, and a better temporary resolution.

2.2 X-ray generation

There are several ways used to produce x-rays which include synchrotron radiation (SR) and laboratory-based x-ray production. Synchrotron radiation is produced when relativistic charged particles are forced by some external magnetic force to bend their trajectories. Synchrotrons have found widespread use in multi-purpose scientific research around the world because they produce high-energy x-rays which makes them efficient for exploring materials structures [4]. In a laboratory setup, however, x-ray production is done through the use of an x-ray tube.

A typical x-ray tube has the following main components which are shown in figure 2.1. The cathode consists of a thin filament that is responsible for discharging the electrons and a tungsten x-ray target that produces the x-rays in a vacuum container tube.

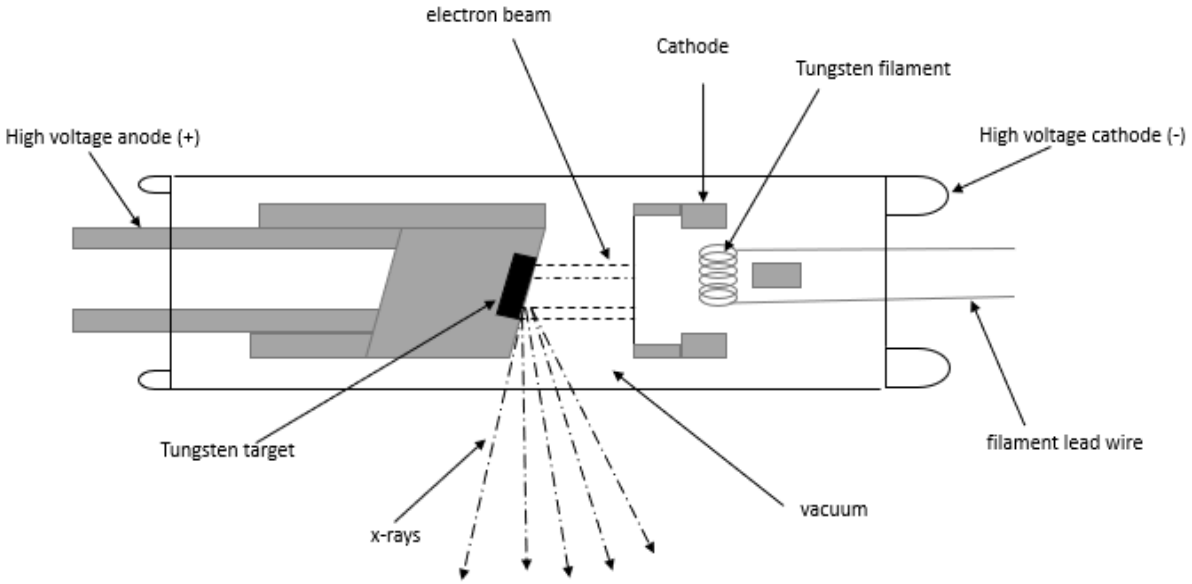

Figure 2.1:Schematic of an x-ray tube structure [2].

When the x-ray machine is turned on, an electrical current passes through the filament and heating occurs due to the resistance in the tungsten wire which results in the emission of electrons through a process known as thermionic emission. This is a phenomenon where if one applies energy to a free electron in the conduction band, the electron overcomes the threshold of forces holding it in the metal, called the work function, and emission occurs. The emitted electrons are then accelerated by a bias voltage to the tungsten anode where they collide with atoms of the tungsten material and produce x-rays. For a highly efficient x-ray tube, the energy of the incoming electrons is converted into x-rays (about 1%) and heat (about 99%) [5]. The amount of heat produced in the x-ray rube affects the efficiency of x-ray production as well as causes damage to the x-ray tube. The Nikon Metrology CT scanner used for this work has an open tube design. With this setup, the x-ray tube only gets evacuated when the machine is powered up. One of the benefits of this design is that failed parts such as filaments are easily replaceable and it is also furnished with water or oil-coolant which are useful in dissipating heat from the x-ray tube [6].

The produced x-rays consist of “characteristic radiation” and Bremsstrahlung radiation, with the latter being the major x-ray production process. Bremsstrahlung x-rays are produced when an incident electron has a collision with an atom of the x-ray target which results in the electron being decelerated because of the repulsive forces from the negatively charged electron cloud

around the nucleus. The kinetic energy lost by the incident electron is emitted as an x-ray photon as shown in figure 2.2 (a). This process produces a continuous x-ray spectrum. On the other hand, characteristic radiation shown in figure 2 (b) is produced when an electron with high energy bombards an atom of the x-ray target and excites an inner shell electron. When the electron goes through a de-excitation process, energy is released and yields a photon of characteristic radiation [7].

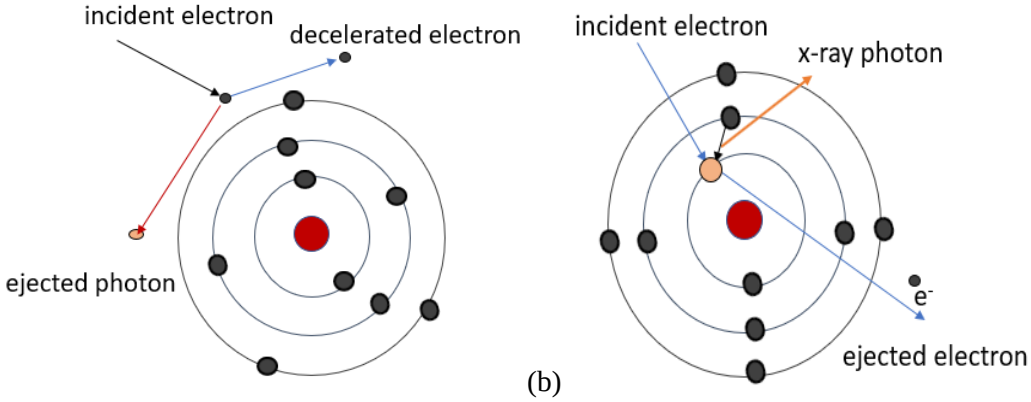

Figure 2.2: Sketch of the process involved in x-ray generation. (a) Bremsstrahlung and (b) characteristic radiation.

This type of energy is characterized by a line spectrum and is shown in figure 2.3 for the tungsten anode material used for this research work.

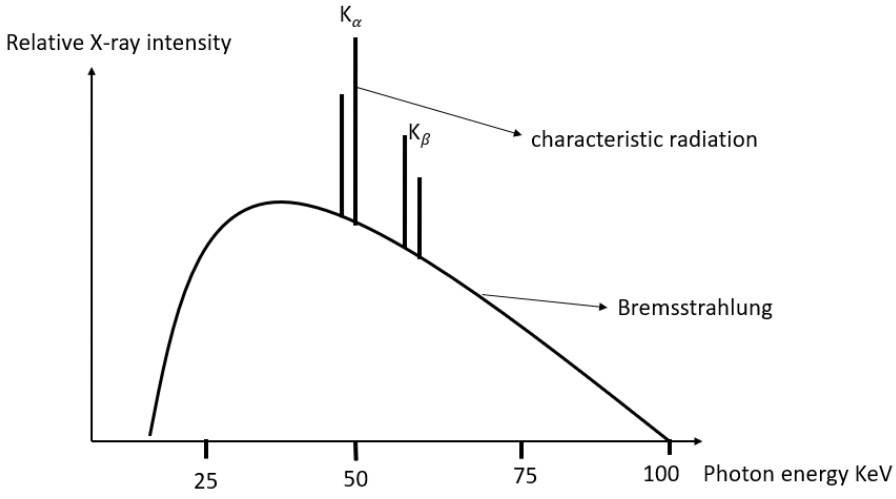

Figure 2.3**:** Bremsstrahlung and characteristic radiation spectra are shown for a tungsten anode with x-ray tube operation at 100 kV.

The probability of Bremsstrahlung radiation is related to the energy of the incoming electron. Low energy electrons have a higher probability of being slowed down during collisions. Figure 2.3 shows two pairs of peaks, where the first pair which corresponds to lower energy is for the K_α (transitions from the L shell to the K shell) and the second pair corresponds to higher energy transitions K_β in which the gap in the K shell is filled by electron coming from two or more shells away. For characteristic radiation, the electron transitions generate x-rays whose energy is the difference between the two layers [7].

X-rays can be described as electromagnetic waves, with the energy of a single photon E_p being directly proportional to its stimulation frequency *v* and given by the equation,

$$E_p = hv = h\frac{c}{\lambda}. \tag{2.1}$$

The constant *h* is called the Planck constant and has the value $h = 6.63\times10^{-34}$Js. The photon energy can also be described in terms of its wavelength and the speed of light represented by the constant *c* whose value is $c = 3\times10^{-8}$m/s. The wavelength of the radiation has a range from 0,01 to 10nm, and the x-rays are either called soft or hard x-rays depending on the level of energy that is attached to their respective wavelengths [7].

2.3 Beam filtering

The attenuation of x-rays in CT is a function of the wavelength, and this affects the quality of the data output. During CT scanning, lower energy x-rays (higher wavelength) tend to be more absorbed or scattered than higher energy x-rays [8]. When this happens, the average energy of the x-rays is shifted towards the hard x-rays which possess higher energies. This energy shift results in beam hardening which causes artefacts in the CT data. Artefacts due to beam hardening will be discussed in chapter 3 which focuses on image reconstruction. Figure 2.4 shows the x-ray spectrum of a tungsten anode. During the x-ray filtering process, a metal usually copper or aluminium filter measuring a few millimeters is placed in front of the x-ray source and filters low-energy x-rays. In addition to increasing the average energy of the radiation, the filtering process reduces beam hardening artifacts during the image reconstruction step [9].

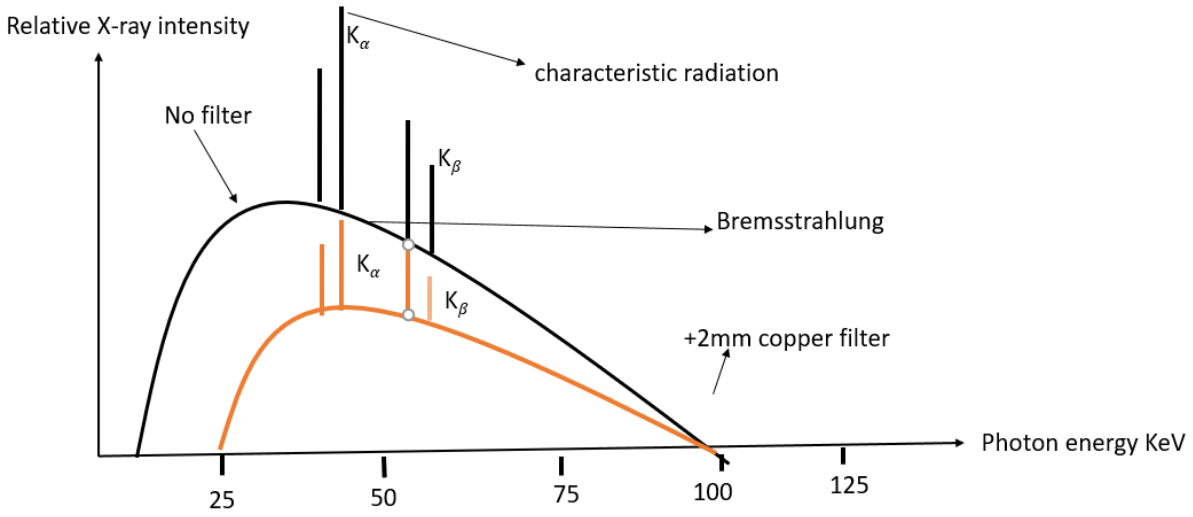

Figure 2.4: Beam hardening of an X-ray spectrum produced by a tungsten anode due to filtering by a 2 mm copper filter.

2.4 Interaction of x-rays with matter

X-rays, interact with matter via photoelectric absorption, Compton scattering, Rayleigh scattering, and pair production [10]. In photoelectric absorption, figure 2.5, all the energy from, an incident photon is absorbed by an electron in an inner shell causing it to be subsequently ejected as a photoelectron. This process takes place at lower photon energy levels and the energy balance equation is given by,

$$hv = E_p = E_b + E_{pe,} \qquad (2.2)$$

where the incident x-ray photon has its energy given as E_p. The electron has a binding energy E_b and the energy of the ejected photoelectron is given by E_{pe}.

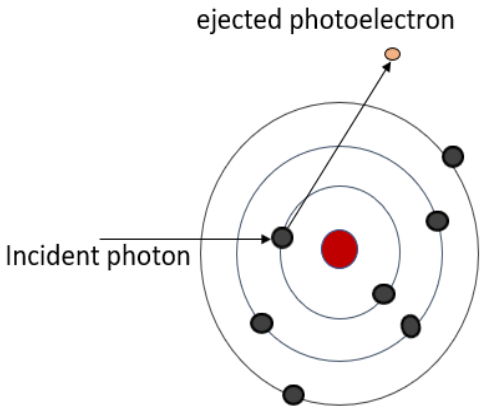

Figure 2.5: Photoelectric absorption

The x-ray photon is absorbed, and the atom stays ionized until the vacant place in the lower shell is refilled. The attenuation due to the photoelectric effect (μ_{pe}) is dependent on the energy of the photons and the atomic number of the object (Z) and is related by the equation,

$$\mu_{pe} \propto \lambda^3 Z^4 \ , \tag{2.3}$$

with the wavelength λ and the attenuation coefficient belonging to a certain energy level of the photons.

In Compton scattering shown in figure 2.6, an incident x-ray photon whose energy is given by E_p interacts with an electron whose binding energy is given by E_b. The electron is subsequently ejected and in the process, the x-ray photon is deflected and loses some energy which is gained by the electron. This process only happens when the incoming photon has more energy than the binding energy of the electron [10].

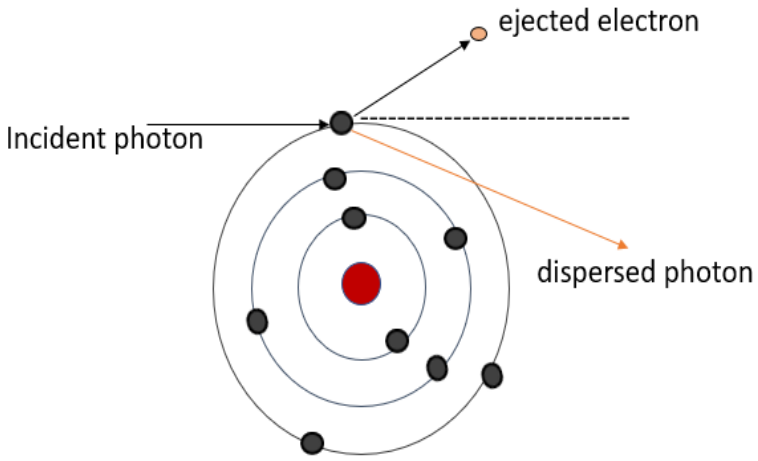

Figure 2.6: Compton scattering process

The energy balance equation is given by:

$$h\nu = E_p = E_e + E_{p'} \tag{2.4}$$

with the energy of the electron involved in the Compton process given by E_e and the energy of the deflected photon given by $E_{p'}$.

For both effects, the probability of an x-ray photon being lost from the original beam is therefore energy-dependent. This implies that the attenuation coefficient depends on both the material density and the x-ray energy [11]. The resulting attenuation coefficient is given by,

$$\mu = \mu_{pe} + \mu_{compton} \ . \tag{2.5}$$

Using this relation, we can state the Beer-Lambert which describes the attenuation of x-rays as they pass through matter. For a monochromatic incident x-ray beam, the ordinary differential equation,

$$\frac{dI}{I\,(x)} = \mu dx, \tag{2.6}$$

is a representation of the spatial evolution of the beam intensity in one dimension. For a homogeneous material with attenuation coefficient μ we obtain,

$$I(x) = I_0 e^{-\mu x}\,, \tag{2.7}$$

with I_0 being the initial intensity of the x-rays and x being the distance the x-rays travel through the object.

The Rayleigh scattering process shown in figure 2.7 which is also known as the Thomson scattering is an elastic event that is observed when the wavelength of the incoming radiation is larger than the diameter of the scattering nucleus [12]. The scattered and the incident radiation both have equal wavelengths, however, the direction of the scattered radiation and the incident radiation is different. This process results in no energy transfer and the Thomson cross-section is derived from the classical model and is given by

$$\sigma_{Thomson} = \frac{8\pi r_e^2}{3}\frac{\omega^4}{\left(\omega^2-\omega_0^2\right)^2} \tag{2.8}$$

Where

$$r_e = \frac{1}{4\pi\varepsilon_0}\frac{e^2}{m_e c^2} \tag{2.9}$$

being a typical classical radius with the permittivity of free space is given by ε_0.

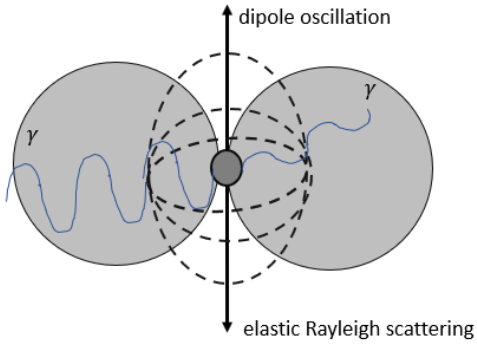

Figure 2.7: principles of photon–matter interaction via the Rayleigh scattering

The atom is bounded by a natural frequency ω_0 and the energy of the incident radiation is given by ω. The probability of scattering is proportional to the fourth power of the radiating frequency and for very low energies where $\omega < \omega_0$, elastic scattering becomes a major contribution to the attenuation of x-rays [12]. For higher frequencies, however, where $\omega \gg \omega_0$, other processes such as the photoelectric effect and the Compton scattering become dominant, whilst the Rayleigh scattering process becomes constant.

The probability of creating electron-positron pairs in the Coulomb field in the nucleus increases with photon energy [13]. For photon energies of $h\nu$ = 1.022 MeV, the energy balance equation for the pair production is given is by,

$$h\nu \rightarrow e^- + e^+ + 2E_{kin}, \tag{2.10}$$

if Einsten's mass-energy equivalency,

$$h\nu = 2m_e c^2 + 2E_{kin}, \tag{2.11}$$

is satisfied. The positron, e^+ possesses the same physical properties as the electron e^-. The only difference is the positron charge which is positive. Figure 2.8 shows that when the positron collides with the electron, they disintegrate and two γ-rays emerge. When these γ-rays finally come to rest, each of these particles has the energy of $m_e c^2$ when the particles come together at rest. This process is called annihilation and is given by the energy balance [13]:

$$e^- + e^+ \rightarrow 2h\nu. \tag{2.12}$$

After annihilation, these two photons travel in opposite directions. In the process, the mass of both the positron and electron is transformed, and the two resulting photons emerge with equal energy of 511 keV.

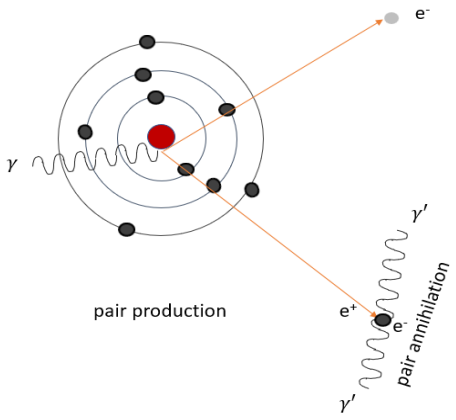

Figure 2.8: Principles of photon–matter interaction via the pair production

The contributions of these four attenuation processes to the total x-ray attenuation depends on the material that is penetrated and the energy of the incident beam. In figure 2.9, the functional behaviour of the total attenuation due to the processes involved in x-ray interaction with matter is given as a function of the quantum energy for lead (Pb) [14]. For energies with $hv > 10\ MeV$, the dominant means of x-ray attenuation is pair production. In the mid- energy range $hv \approx 1MeV$, the Compton scattering becomes dominant. The photoelectric effect governs the overall behaviour in the CT diagnostic energy window 50keV $\leq hv \leq$ 140keV [15]. For the Rayleigh scattering, its contribution to the total attenuation is more than one magnitude lower than the desired x-ray photon absorption.

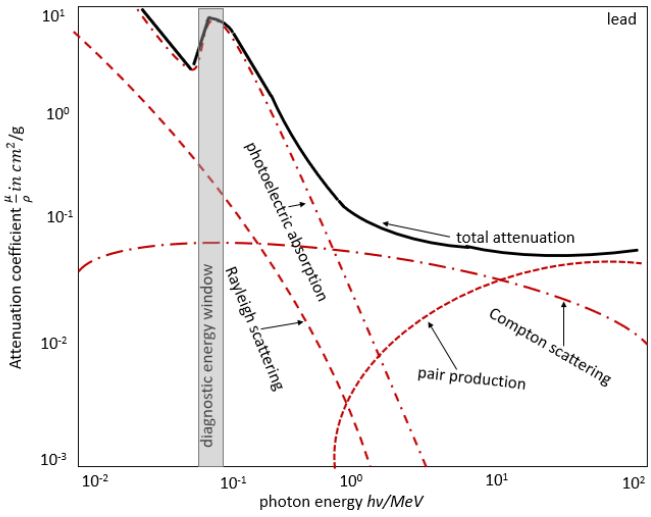

Figure 2.9: Mass attenuation coefficient, μ/ρ, versus incident photon energy for Pb [14].

2.5 X-ray detection

The main interaction principles between X-ray photons and matter have been explained in the section above. X-ray quanta are not measured directly but rather detected via their interaction products like the emitted photoelectrons. The overall efficiency of the detection of x-rays is determined by quantum efficiency and geometric efficiency. Quantum efficiency refers to the fraction of incident x-rays that are absorbed and contribute to the total signal. The geometric efficiency refers to the x-ray sensitive area of the detector as a fraction of the total exposed area [16].

2.5.1 Gas detectors

X-rays are able to ionise gases and as of today, CT scanners using high-pressure xenon are in use. The photoelectric interaction

$$hv + Xe \rightarrow Xe^{+} + e^{-} \qquad (2.13)$$

describes the first part of the detection process. The Xenon ions are attracted to the cathode and the electrons are attracted to the anode by a high voltage. A series of alternating anode and cathode pairs form the detector array [16]. Figure 2.10 shows the reaction chain which starts with the photoelectric ionization and ends with the free charged particles recombining at the electrode surfaces. During the recombination process, a current is produced which provides a measure of the intensity of x-rays reaching the detector.

Tall ionization chambers and high pressure provide compensation for a low probability of photoelectric absorption. Tall ionisation chambers also improve the directional sensitivity of the detector element. The ionisation probability is directly proportional to the distance traveled by the x-ray quanta inside the detector element [17]. The detector element has built-in collimation which suppresses x-ray quanta with an oblique entrance.

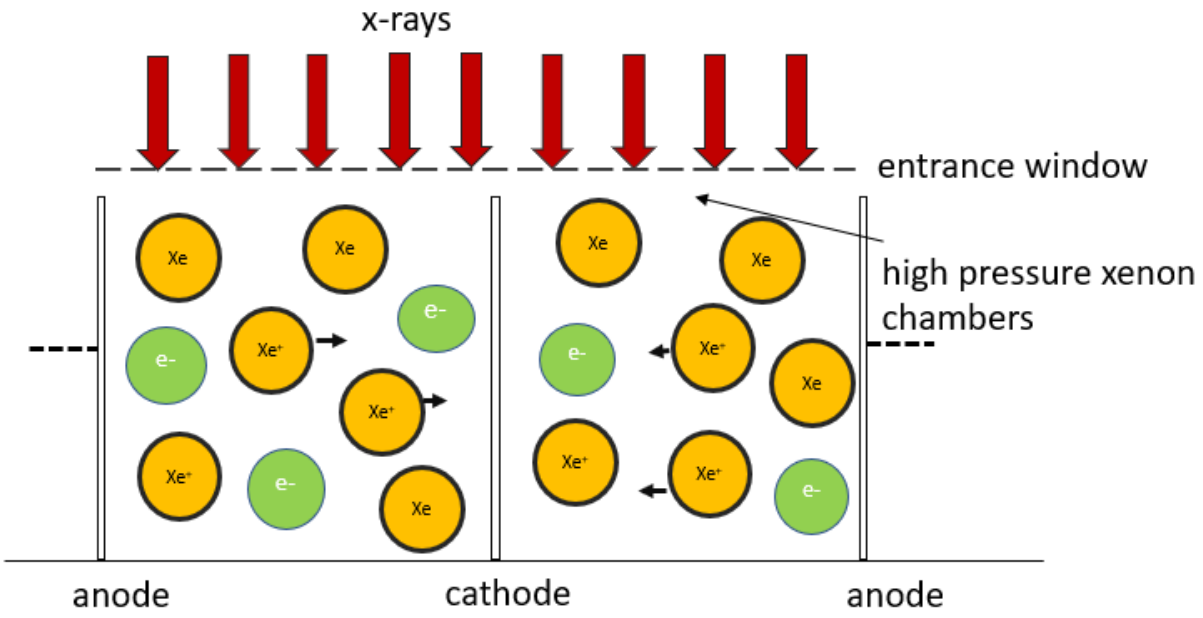

Figure 2.10: Schematic cut-out of two adjacent ionizing chambers of a xenon high-pressure detector array. Since the chambers are communicating, all detector elements have the same Xe pressure and, therefore, the same sensitivity.

2.5.2 Solid-state scintillator detector

The most important components of a scintillator detector are a scintillator medium and a photon detector. The x-rays incident on the detector are converted into light in the scintillation media. The choice of scintillator material depends on the desired efficiency for the conversion of x-rays into light and the time taken for the conversion process also known as a time constant. Typical scintillator materials that are used are cesium iodide (CsI) [17].

For a very small-time constant which is required by modern CT scanners, ceramic materials such as the ones made of gadolinium oxysulphide (Gd_2O_2S) are used [18]. The mass attenuation coefficient of the detector material must be known so as to assess the quality of the detector material with respect to the high quantum efficiency which is desired. Figure 2.11 shows that the Gd_2O_2S ceramic possesses a higher probability of energy conversion through the photoelectric effect compared to xenon. The mass density ρ of the gas xenon is 3 magnitudes lower than the mass density of the solid-state detector, and hence the effective absorption of x-rays inside the solid-state detector and therefore its quantum efficiency is also high.

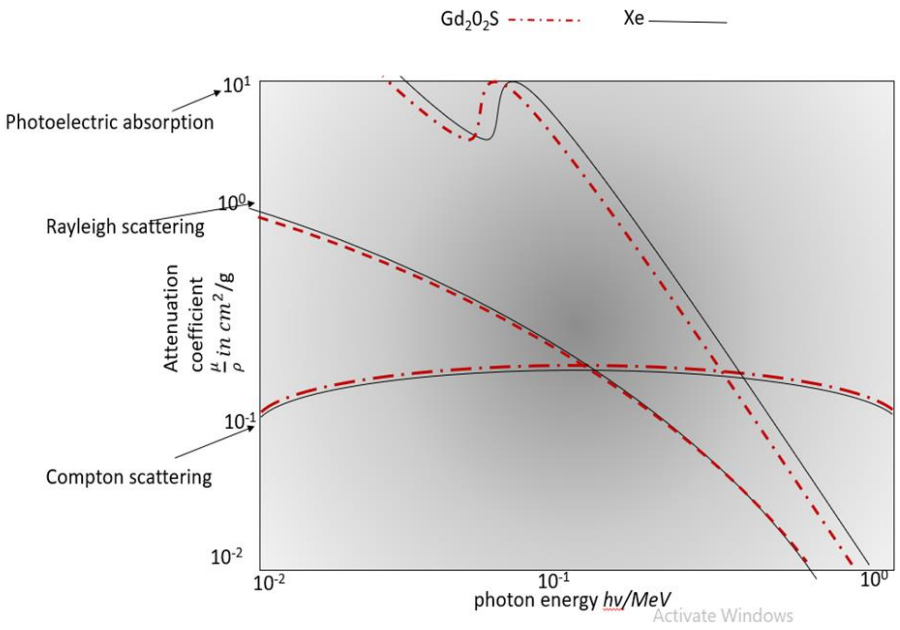

Fig 2.11. Mass attenuation coefficient for the main photon–matter interaction principles in detector materials. Photoelectric absorption is more than one magnitude higher than scattering processes in xenon and the Gd_2O_2S ceramic [14].

Figure 2.12 shows the components of a scintillator detector unit. Each detector unit consists of individual detector elements. Scattered x-rays undergo a small angle deflection before they finally reach the detector. This process is undesired as it reduces contrast in CT data. To suppress these deflections, the detector has anti-scatter collimators which are attached to each of the available detector elements. These anti-scatter collimator grids are directed towards the x-ray focus and their job is to ensure that photons that are not traveling in the line of sight between the x-ray source and the detector are filtered out [19].

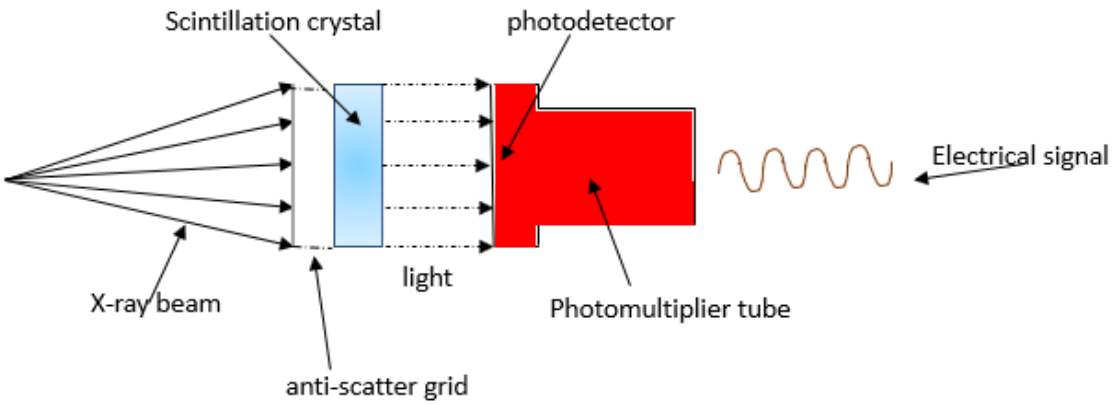

Figure 2.12: Schematic of a scintillator x-ray detector

2.5.3 Solid-State Flat-Panel Detectors

Of particular importance to this work is this flat panel detector type shown in figure 12 which is used in our XCT machine. The detector used is a PerkinElmer 16-inch amorphous silicon(a-Si) digital x-ray detector operating as a 2-dimensional photodiode array which is equipped with a cesium iodide (CsI) scintillator illustrated in figure 2.12.

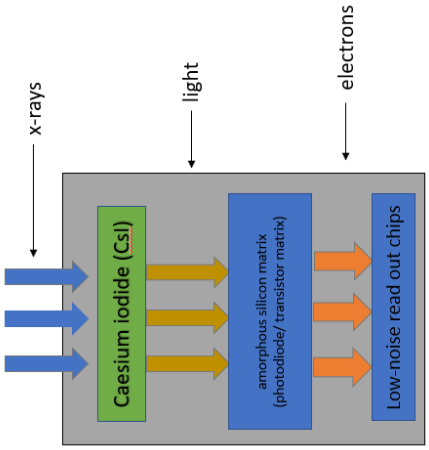

Fig 2.12**:** Schematic of a digital flat-panel X-ray detector.

Behind the CsI layer, there is a photodetector which functions as an electronic light sensor. The visible light is absorbed, and electrons are emitted into the photomultiplier tube using the photoelectric effect. Inside this photomultiplier tube, the electrical information is aligned and multiplied using layers of diodes. In the end, the electrical signal is transmitted to digital backend devices where it is converted to grey value images [20]. These grey value images represent the average x-ray intensity for each pixel area. Each sensor element has a thin film transistor (TFT) and a photodiode. Both the TFT and the photodiode are made of amorphous silicon on a single glass substrate. The pixel matrix [20] has an x-ray sensitive area that is coated with a cesium iodide layer. Multi-chip modules are used as read-out electronics at the edge of the detector field.

The read-out process is initialised by the TFT which switches the charge to the read-out electronics via the data link. Amplification of the analog to digital conversion is performed on the same chip resulting in a fast operation with noise.

2.5.4 Properties of XCT detectors

High quantum efficiency is required for the conversion of x-rays into light pulses**.** For this reason**,** the choice of scintillation material has a great influence on the projection image quality, and hence it is very important. The choice of material also determines stability over time, detection efficiency, and sensitivity [21]. The presence of a sensor circuitry in the detector which is adjacent to each pixel makes a fraction of the display area which is called the dead region to be insensitive to radiation. This area is in turn not used for CT data analysis. The radiation is supposed to interact with the detector in a manner that produces a useful signal. The probability η of an x-ray photon interacting with the detector is given by the equation,

$$\eta = 1 - e^{(-\mu(E)T)}. \quad (2.14)$$

Where E is the energy of the photon, $\mu(E)$ is the detector's linear attenuation and T is the thickness of the detector [22]. When an x-ray beam passes through a specimen, low-energy photons are attenuated, and this results in beam hardening. The remaining photons have higher energy which gives higher efficiency for the scintillation processes. This means that the detector efficiency should be calibrated over a range of frequencies. This efficiency is directly proportional to the thickness of the detector and can be increaed by using materials with a higher attenuation coefficient because of the increased density. This is explained by the fact the detection of the x-ray beam is dependent upon the photon interactions with the nucleus of the material in the detector [21]. The greater the distance an x-ray photon traverses through the material, the greater the probability it has to interact with at least one atomic nucleus.

Photo-detectors have a linear response which is defined for a finite range of input signal energy. The CsI detector used in this research work has a dynamic range of $> 77dB$. Outside this range, the detector either gives no response to x-rays at all or becomes non-linear [23]. For example, if the incident photon energy is too low, it does not pose enough energy to displace an electron and hence no signal is observed. Similarly, if there were an insufficient number of photons, the probability of a collision occurring would be too small even if the photons have sufficient energy to generate a signal. This signal would be lost as noise and would be termed the noise equivalent input since the lower level of this signal cannot be distinguished from the detector noise [24]. For the case where the incoming photons have higher energy or their number is large, the detector may be unable to distinguish between two adjacent photons resulting in detector saturation.

The variation of response to a spatially uniform and constant x-ray illumination across the face of the detector receptor area is called uniformity. For the Nikon meteorology CT scanning machine, areas where the detector does not have the same sensitivity, are corrected in the Inspect-X software by doing a pixel response mapping and correction [24]. The PerkinElmer 16-inch amorphous silicon(a-Si) digital x-ray detector has a pixel response non-uniformity of $\pm 2\%$ (10% to90% film screen radiography).

References: Chapter 2

1. Panchbhai, A.S., 2015. Wilhelm Conrad Röntgen and the discovery of X-rays: Revisited after centennial. *Journal of Indian academy of oral medicine and radiology*, *27*(1), p.90.
2. Elke, M., 1995. One century of diagnostic imaging in medicine. *Experientia*, *51*(7), pp.665-680.
3. Wells, P.N.T., 2001. Physics and engineering: milestones in medicine. *Medical engineering & physics*, *23*(3), pp.147-153
4. Strüder, L., Epp, S., Rolles, D., Hartmann, R., Holl, P., Lutz, G., Soltau, H., Eckart, R., Reich, C., Heinzinger, K. and Thamm, C., 2010. Large-format, high-speed, X-ray pnCCDs combined with electron and ion imaging spectrometers in a multipurpose chamber for experiments at 4th generation light sources. *Nuclear Instruments and Methods in Physics Research Section A: Accelerators, Spectrometers, Detectors and Associated Equipment*, *614*(3), pp.483-496.
5. Li, Y., Sun, Y. and Yeow, J.T.W., 2015. Nanotube field electron emission: principles, development, and applications. *Nanotechnology*, *26*(24), p.242001.
6. Valone, T. ed., 1995. *Electrogravitics Systems: Reports on a new propulsion methodology* (Vol. 1). Integrity Research Institute.
7. Sempau, J., Acosta, E., Baro, J., Fernández-Varea, J.M. and Salvat, F., 1997. An algorithm for Monte Carlo simulation of coupled electron-photon transport. *Nuclear Instruments and Methods in Physics Research Section B: Beam Interactions with Materials and Atoms*, *132*(3), pp.377-390.
8. Kandarakis, I., Cavouras, D., Sianoudis, I., Nikolopoulos, D., Episkopakis, A., Linardatos, D., Margetis, D., Nirgianaki, E., Roussou, M., Melissaropoulos, P. and Kalivas, N., 2005. On the response of Y3Al5O12: Ce (YAG: Ce) powder scintillating screens to medical imaging X-rays. *Nuclear Instruments and Methods in Physics Research Section A: Accelerators, Spectrometers, Detectors and Associated Equipment*, *538*(1-3), pp.615-630.
9. Meganck, J.A., Kozloff, K.M., Thornton, M.M., Broski, S.M. and Goldstein, S.A., 2009. Beam hardening artifacts in micro-computed tomography scanning can be reduced by X-ray beam filtration and the resulting images can be used to accurately measure BMD. *Bone*, *45*(6), pp.1104-1116.
10. Hubbell, J.H., 1999. Review of photon interaction cross section data in the medical and biological context. *Physics in Medicine & Biology*, *44*(1), p.R1.
11. Alvarez, R.E. and Macovski, A., 1976. Energy-selective reconstructions in x-ray computerised tomography. *Physics in Medicine & Biology*, *21*(5), p.733.
12. Grießhammer, H.W., McGovern, J.A., Phillips, D.R. and Feldman, G., 2012. Using effective field theory to analyse low-energy Compton scattering data from protons and light nuclei. *Progress in Particle and Nuclear Physics*, *67*(4), pp.841-897.
13. Hubbell, J.H., 2006. Electron–positron pair production by photons: A historical overview. *Radiation Physics and Chemistry*, *75*(6), pp.614-623.
14. Berger, M.J, Coursey, J.S, Zucker, D.S ESTAR, PSTAR, and ASTAR: Computer programs for calculating stopping-power and range tables for electrons, protons, and helium ions (version 1.2.2). National Institute of Standards and Technology,

Gaithersburg; Available from http://physics.nist.gov/PhysRefData/Star/Text/contents.html
15. Danad, I., Fayad, Z.A., Willemink, M.J. and Min, J.K., 2015. New applications of cardiac computed tomography: dual-energy, spectral, and molecular CT imaging. *JACC: Cardiovascular Imaging*, *8*(6), pp.710-723.
16. Seibert, J.A. and Boone, J.M., 2005. X-ray imaging physics for nuclear medicine technologists. Part 2: X-ray interactions and image formation. *Journal of nuclear medicine technology*, *33*(1), pp.3-18.
17. Hermanek, P., Rathore, J.S., Aloisi, V. and Carmignato, S., 2018. Principles of X-ray computed tomography. In *Industrial X-Ray Computed Tomography* (pp. 25-67). Springer, Cham.
18. Belev, G. and Kasap, S.O., 2004. Amorphous selenium as an X-ray photoconductor. *Journal of non-crystalline solids*, *345*, pp.484-488.
19. Tizpar, A., Satkin, M., Roshan, M.B. and Armoudli, Y., 2014. Wind resource assessment and wind power potential of Mil-E Nader region in Sistan and Baluchestan Province, Iran–Part 1: Annual energy estimation. *Energy conversion and management*, *79*, pp.273-280.
20. Janesick, J.R., 1997, April. CCD transfer method: standard for absolute performance of CCDs and digital CCD camera systems. In *Solid State Sensor Arrays: Development and Applications* (Vol. 3019, pp. 70-102). International Society for Optics and Photonics.
21. Granfors, P.R., Aufrichtig, R., Possin, G.E., Giambattista, B.W., Huang, Z.S., Liu, J. and Ma, B., 2003. Performance of a amorphous silicon flat panel x-ray detector designed for angiographic and R&F imaging applications. *Medical physics*, *30*(10), pp.2715-2726.
22. Martin, T. and Koch, A., 2006. Recent developments in X-ray imaging with micrometer spatial resolution. *Journal of synchrotron radiation*, *13*(2), pp.180-194.
23. Yin, W., Hu, P., Indulska, J., Portmann, M. and Mao, Y., 2020. MAC-layer rate control for 802.11 networks: A survey. *Wireless Networks*, *26*(5), pp.3793-3830.
24. Kennel, M.B. and Isabelle, S., 1992. Method to distinguish possible chaos from colored noise and to determine embedding parameters. *Physical Review A*, *46*(6), p.3111.

Chapter 3: Image reconstruction

3.1 Introduction

In this chapter, our focus is on a set of geometrical setups for micro-CT scanning. The parallel beam scanning setup in section 3.1 serves as a theoretical interest for reconstruction fundamentals. The fan beam scanning scenario is the preliminary stage of the 3D cone beam scanning setup which is used in our x-ray micro-CT system. This chapter also focuses on the image reconstruction algorithms that can be chosen and used inside the ASTRA toolbox. Our particular interest is in algebraic reconstruction methods such as the SIRT which can serve as an alternative to the FBP algorithm.

3.2 Parallel beam tomography

Figure 3.1 shows a parallel beam tomography schematic, which is mainly used at synchrotron sources. The black circle in the middle is a representation of the object under investigation. The cartesian coordinate system is fixed in its centre with the e_x and e_y axis lying in the paper plane. To obtain a set of projection images, the object is rotated around the e_z – axis in a counter-clockwise direction. The vectors *s* and *d* point from the x-ray source to the centre of the object and the centre of the object to the middle pixel in the detector respectively. The length d_{so} represents the distance from the x-ray source to the origin of the coordinate system d_{so} ($d_{so} = \|s\|_2$) and d_{od} represents the distance from the origin of the coordinate system to the centre of the detector d_{od} ($d_{od} = \|d\|_2$).

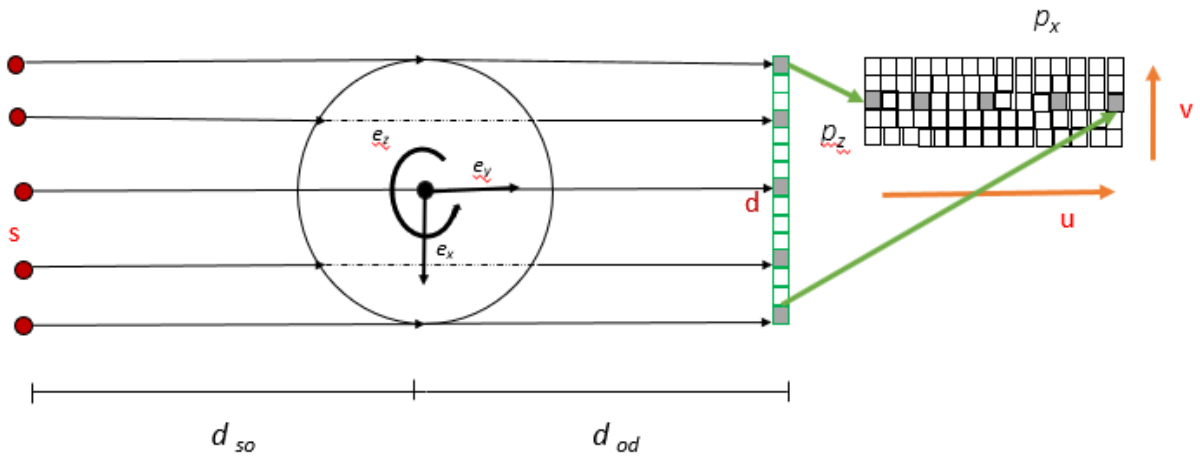

Figure 3.1: A schematic of parallel beam tomography.

In 3D parallel beam tomography, the intensity of the x-rays reaching the detector is measured on a strip of detector pixels with the detector having a rectangular grid of $N_x \times N_z$ pixels with the same dimensions $p_x \times p_z$. The pair of vectors {u, v} are a representation of the spatial orientation of the detector's surface related to the given Cartesian coordinate system. They indicate the vector from the central pixel to the next pixel in the horizontal and vertical directions respectively.

3.3 Fan beam geometry

Fan beam tomography is sometimes used in medical CT scanners and figure 3.2 shows a schematic. The point s is the x-ray source, then the black dot in the middle represents the position of the sample and at a distance $d_{SO} + d_{Od}$ from the source is the detector. The x-ray source is assumed to be a point source from which the x-rays are released in a fan shape.

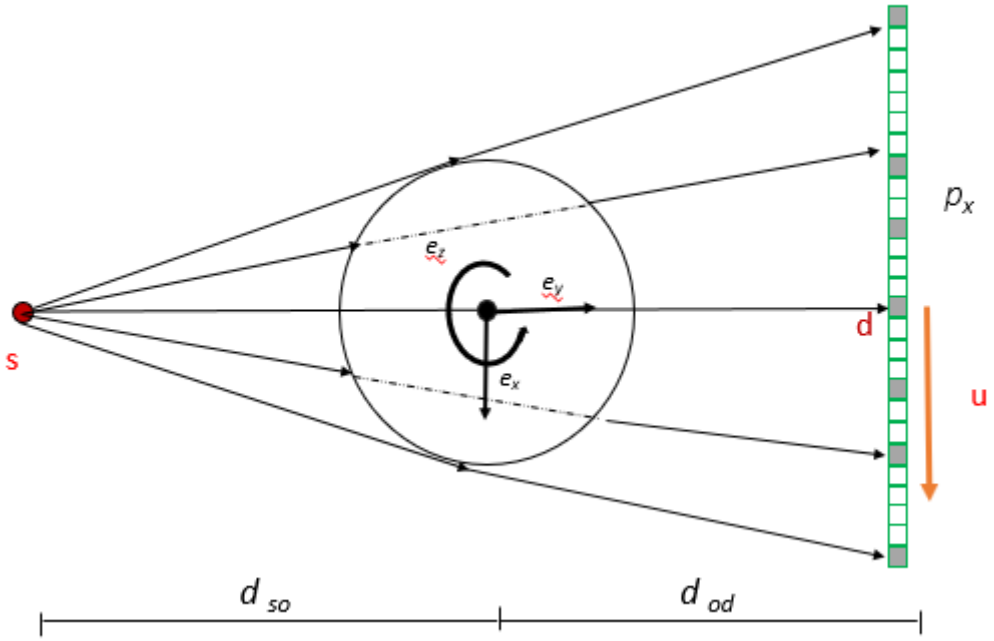

Figure 3.2: Simplified representation of a fan beam scanning scenario

In this setup, the object under investigation is enlarged through geometric magnification *(M)* and is quantified by the equation,

$$M = \frac{d_{so} + d_{od}}{d_{so}} = \frac{d_{sd}}{d_{so}}. \qquad (3.1)$$

This version uses equal-spaced fan-beam scanning for a flat detector array that has equal spacing p_x. Quite contrary to this is the idea of an equiangular fan-beam geometry with a curved

array of detector elements, where the angle between two neighbouring rays is constant over the total opening angle and all X-ray beams have the same length.

3.4 Cone-beam geometry

Cone beam geometry is obtained when a cone-shaped photon beam is produced as shown in figure 3.3. For this setup, the beam is produced in the x-ray tube and a flat panel detector is introduced as a replacement for the multi-line detector arrays which gives this geometry the ability to acquire more images in a short time. The x-ray measuring field is usually $2cm^3$ in volume and hence these CT scanners are more popular in material analysis and testing [1].

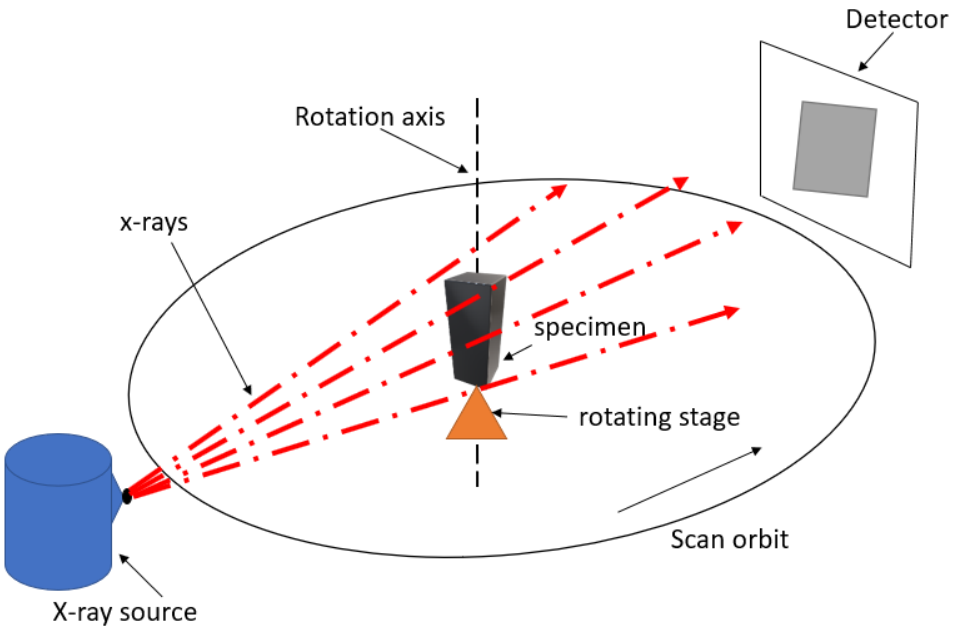

Figure 3.3: Schematic of cone-beam x-ray computed tomography.

Although the sizes d_{so} and d_{od} are not shown in the image, they are given as the Euclidean norm of vectors of the x-rays that pass through from the middle of the x-ray source to the centre of the detector array which can also be referred to as an optical axis. The geometric magnification M in this case additionally defines the resulting voxel size V_x which shows the internal structures of the specimen in 3D and is given by,

$$V_x = \frac{p_x}{M}. \tag{3.2}$$

The flat panel detector measures and digitally records the x-ray attenuation for the specimens scanned. For each angle, a 2D radiograph is obtained. However, it is not possible to determine

the distribution of the attenuation coefficients of the specimen from these single radiographs. That is, when there are homogenous samples arranged one after the other as shown in figure 3.4 below, the radiograph shows the attenuation of the x-ray beam intensity after passing through all three samples. However, if we rotate the sample stage through ninety degrees we are able to distinguish the three samples on the radiograph. Computed tomography allows one to view the specimen from all sides since the object rotates from 0º to 360º as radiographs, also referred to as projections, are collected [2].

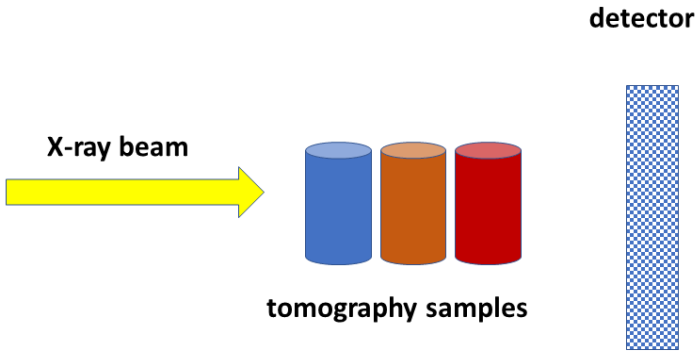

Figure 3.4: Three samples arranged in line with the direction of the x-ray beam towards the detector.

3.5 Computed tomography kinematic systems

In our micro-CT setup, the specimen rotates without translational movement in the space between the x-ray source and the detector whilst the x-ray source and detector remain in fixed positions. The kinematic system of the CT scanner used for this work has the following components:

1. A sample stage is used to rotate the specimen continuously or stepwise.
2. A horizontal translation axis is located between the x-ray source and detector. It is used to place the sample stage with the specimen. The axis is used for magnification, with a higher magnification obtained when one places the specimen nearer to the x-ray source thereby increasing the image resolution [3].
3. A vertical translation axis which is used for moving the sample stage in the Z direction. In the case of tall specimens, it is then used to position a specific region of the specimen in the measuring field.
4. There is also another horizontal translation axis that moves the sample stage in a parallel direction to that of the x-ray detector. This movement aids for the sample stage positioning in and outside the field of measurement.

3.6 Software

The XCT software is important in the reconstruction of 3D data from the acquired 2D projections. As stated before, the most common method for 3D volume reconstruction is the filtered-back projection (FBP). In 1917, John Radon proved that an image of an unknown object could be formed if one had an infinite number of projections passing through the object. The input for the reconstruction is “grey value profiles” which represent the variation in x-ray intensity in each pixel on the detector. The resolution of the reconstruction is influenced by the number of pixels in each grey value profile, the pixel size, the number of projections taken in one angular pose, and the number of angles from which the projections are obtained. More details of this are covered later in section 3.9 when discussing the image reconstructions using the ASTRA toolbox.

3.7 The problem of image reconstruction: CT artefacts

The choice of the reconstruction algorithm can influence the quality of data obtained from a CT scan. The FBP algorithm can have limitations such as beam hardening, scatter, and noise, and in some cases the source of these are the parameters chosen for tomography or the nature of the sample or some limitations in the instruments used. These artefacts are discussed in the following sections and illustrated in figures 3.5, 3.6, 3.7, and 3.8.

3.7.1 Metal artefacts

Metal streak artefacts are caused by multiple mechanisms related to the metallic inclusion itself as well as metal edges [4]. They are due to the presence of sub-volumes that are denser, and which attenuate more x-rays as compared to the rest of the contents of a particular specimen. The metal causes Poisson noise, beam hardening, and scatter effects [4]. These artefacts are observed as bright and dark streaks as shown in figure 3.5. These metal artefacts are more commonly pronounced with high atomic numbers and in some instances, the metal edges cause streaks due to under-sampling.

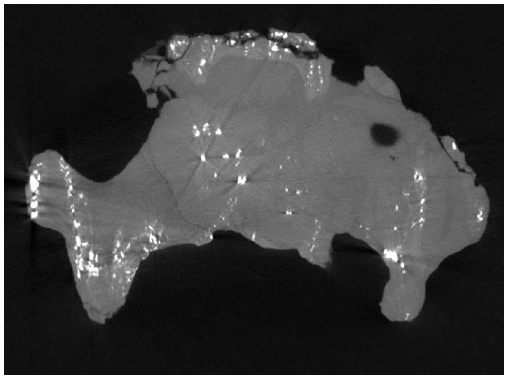

Figure 3.5: A cross-section of an image 3D rendering after reconstructing tomographic projections of a palaeontological specimen with metallic inclusions.

As observed, the specimen has a high fraction of metallic inclusions which appear as the bright regions in the cross-sectional image shown in figure 3.5. Dark and bright streaks can be observed around the slice because of these effects caused by the metallic inclusions. If these metallic inclusions are found in the regions of interest, they make the data less usable as the amount of information that can be derived on the morphology can become limited.

3.7.2 Scatter radiation and beam hardening artefacts

Beam hardening is more pronounced in CT data obtained by using polychromatic x-ray sources. During CT scanning, low-energy photons are absorbed more easily than high-energy photons [5]. After the x-rays have travelled through a particular distance into the specimen, most of the low-energy photons are absorbed and only the high-energy photons will penetrate the specimen density through to the detector. The first few millimetres (mm) of the specimen absorb more x-rays than the interior part which tends to attenuate the remaining high-energy photons. This effect is observed in CT reconstructed datasets where the outer skin of the specimen under investigation appears much brighter than the core of the specimen. Figure 3.6 shows a CT scan of a skull of the fossil primate *Rooneyia viejaensis*. The darkening in the thin central part of the fossil indicated by the arrow in red is a result of beam hardening, as it is also the center of the longest beam paths through solid material.

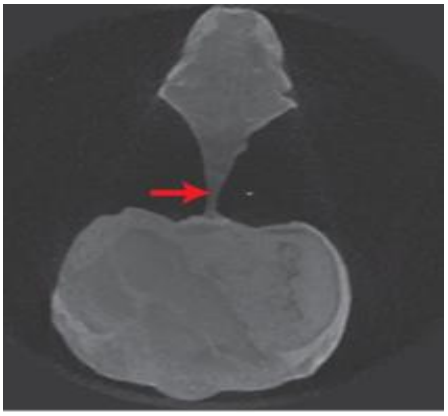

Figure 3.6: A cross-section of 3D rendering from a CT scan of a skull of the fossil primate *Rooneyia viejaensis* showing beam hardening effects.

For low-energy photons, the most common method of interaction is the photoelectric effect, which is defined by the atomic number and the energy of the photons. It is proportional to Z^3/E^3 with Z being the atomic number and E the energy [5]. At higher energies, the Compton scattering process is the primary mode of attenuation and is directly proportional to *1/E*. This interaction results in the x-rays changing their direction thereby ending up in a different region of the detector. When scattered x-rays end up in a detector array that is supposed to have very few photons, errors in the form of artefacts are introduced.

For highly attenuated photon beams, scatter and beam hardening both cause a higher number of photons than expected to be detected. On the other hand, if high-density inclusions in a specimen block all the photons, the corresponding detector element only detects scattered photons resulting in a poor-quality image [5].

3.7.3 Noise

Figure 3.7 shows a cross-section of a 3D rendering from tomographic projections of a dinosaur coprolite with a significant amount of noise. This is due to various causes which include amplification of signals as well as electronic noise of the detector [5], but the most common causes of noise is due to collecting fewer than optimal projections and also having a very small amount of x-ray photon flux reaching the detector after passing through the sample. Poisson noise is produced by the statistical error of low photon counts and results in dark and bright streaks that appear along the direction of the greatest attenuation. In FBP, the projections are filtered to sharpen edge data and then subsequently back-projected. This process does not consider the fact that low photon counts at the detector can result in larger Poisson errors by assuming accurate projection data [5].

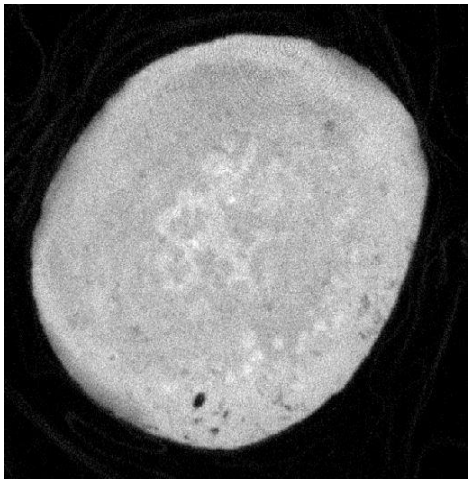

Figure 3.7: A cross-section of a 3D rendering from tomographic projections of a dinosaur coprolite showing the noise which is observed from how grainy the image is.

Noise in the reconstructed CT data of the coprolite was introduced by random variations in detected x-ray intensity that are inconsistent with the projection data. In this project, our implementation of iterative reconstruction methods improves the quality of the CT data by making use of a statistical model to reduce the noise on every iteration performed.

3.7.4 Ring artefacts

Ring artefacts are caused by either defective or mis-calibrated detector pixels [6]. These artefacts appear as rings centred around the centre of rotation as shown in figure 3.8. The remedy is making use of ring minimization where after each rotation to collect the next projection, the sample is moved laterally by a random number distance. However, because of the two motions required for each projection, it increases the time of the scan significantly.

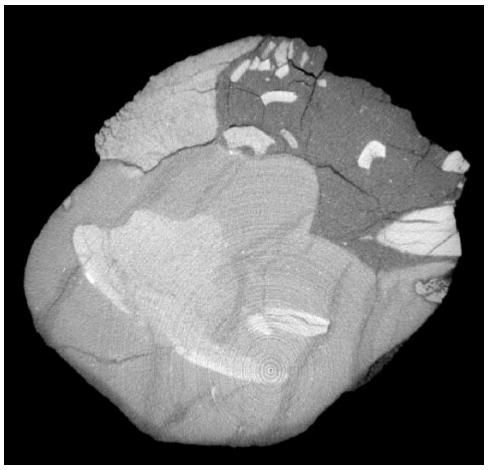

Figure 3.8: Ring artefacts from a cross-section of 3D rendered data of a sample after reconstructing from 2D projections.

By default, the number of projections collected by our instrument is 3142 because the image we reconstruct has 6283 pixels at the circumference. Ideally, we want at least 1 projection per pixel at the circumference which ensures the resolution is homogeneous in our slices (smallest feature visible). Looking at our slices, each projection contributes to diametrically opposed pixels on the slice. The circumference is 1000pixel radius × π × 2= 6283. But as each projection sees two diametrically opposed voxels, the CT system considers that it is fine to have half the number (6283/2 => ~3142). If the sample is smaller than the full diameter of the slice, the number of projections can be decreased which will reduce the extra motor time used for minimising ring artefact (plus the exposure time of each projection).

In a bid to reduce these artefacts in CT data, we implement algebraic reconstruction techniques which will be discussed in the next section as an alternative to the FBP.

3.8 Algebraic reconstruction methods

Algebraic reconstruction methods reconstruct the object's attenuation coefficients using projection data obtained by measuring with an x-ray detector. These reconstruction techniques encompass a set of projections and recovery operations called iterations. During each of the iterations, an estimated sinogram is generated by comparing the projection of the section obtained in the previous iteration to the sinogram measured. The sinogram estimated is then rebuilt by the next iteration up until a new estimate is provided. This process is repeated until the algorithm has converged (when the difference between the estimated and the measured sinogram is smaller than the desired limit).

As stated before, the Radon transform is the basis for all the CT image reconstruction algorithms. The problem of the simultaneous iterative reconstruction technique is illustrated by a single equation,

$$Wv = p. \tag{3.3}$$

(i) $W = w_{ij} \in \mathbb{R}^{M\times N}$ resembles the projection matrix. Hence, entries denoted by $w_{ij=}(W)_{ij}$ represent the length of intersection between a photon i and an image pixel j.

(ii) $v_i \in \mathbb{R}^N$ represents the image vector which encompasses the grey values for every single pixel after reconstruction

(iii) $p_i \in \mathbb{R}^M$ represents the projection vector. M is the product of *D*, the number of detector pixels, and N_p the number of projection views. For this algorithm, p_i is a

representation of a single projection beam (i = 1,……, M) and p_I represents all x-ray beams corresponding to one view, that is $p_I \in \mathbb{R}^D$.

Equation 3.3 has an algebraic forward projection of known voxel data onto specific projection data. The opposite procedure which starts from some given projection information is denoted as a back projection and is shown by the equation

$$u = W^T p. \tag{3.4}$$

This equation does not recover the full voxel information as is in the case for analytical reconstruction. However, the goal of the iterative reconstruction is to find

$$v^* = W^{-1} p. \tag{3.5}$$

The projection matrix W^T is however too big to invert algebraically and the solution to this problem is to set up the optimization problem

$$v^* \in \mathbb{R}^n \; so \; that \; v^* = \; arg \min_{v \in \mathbb{R}^n} \|p - Wv\|^2 \tag{3.6}$$

which searches for the voxel vector $\boldsymbol{v}^*$ which will, in turn, minimise the projection distance to be chosen to vector norm$\|\bullet\|$.

Our focus is on algebraic reconstruction techniques is on the SIRT is motivated by its availability for cone-beam reconstruction in the ASTRA toolbox.

3.8.1 Simultaneous iterative reconstruction technique (SIRT)

According to Gregor and Benson, we can introduce an iteration to update the i-th estimation of the attenuation coefficient vector of the voxels' $\boldsymbol{v}^{(i)}$ to the (i+1)-st step by the use of the SIRT algorithm,

$$v_j^{(i+1)} = v_j^{(i)} + \frac{\sum_{k=1}^{m}\left[w_{kj}\left(p_k - \sum_{i=1}^{n} w_{kl} v_l^{(i)}\right) / \sum_{i=1}^{n} w_{kl}\right]}{\sum_{k=1}^{m} w_{kj}}$$

$$\leftrightarrow v^{(i+1)} \; = \; v^{(i)} + CW^T R \; (p - Wv^{(i)}). \tag{3.7}$$

where the current iterated projection distance p – $Wv^{(i)}$ is concatenated with a particular sequence of matrix multiplications, with C and R being diagonal matrices of the projection matrix **W** that contain the inverse column sum $c_{jj} = 1/\sum_{k=1}^{m} w_{kj}$ and the inverse row

sum$r_{kk} = 1/\sum_{k=1}^{m} w_{kl}$ respectively. The SIRT algorithm given in equation 3.7 solves an optimisation problem as follows:

Iterations start with $\boldsymbol{v}^{(\mathbf{0})}$ =0. The update equation then does the following things.

1. The current reconstruction $\boldsymbol{v}^{(i)}$ is forward projected: $W\boldsymbol{v}^{(i)}$.
2. The result is subtracted from the original projections: $(p - Wv^{(i)})$
3. This difference is then back-projected. In essence, this is done by multiplying with W^T but weighted with C and R.
4. This results in the correction factor $CW^TR\ (p - Wv^{(i)})$**.**
5. The correction factor is then added to the current reconstruction, and the whole process is repeated from step 1.

One of the major problems of iterative methods is the increased computational effort and time which is required to perform multiple iterations, and this is solved by the implementation of graphical processing units.

3.9 Graphics Processing Units

The development and implementation of the graphics processing unit (GPU) based algorithms in CBCT can ensure the fast reconstruction of quality images. A GPU is a computer processer chip that is integrated into a graphics card and can be used to perform rapid mathematical calculations in the iterative image reconstruction process. It is possible to undertake parallelized processes on GPU's for intensive computations which are very essential for computer graphics [7]. In these circumstances, the same kernel or program is executed on many data elements simultaneously and hence it speeds up the reconstruction process for large data volumes. GPUs also enable fast algorithms to reconstruct high-quality images obtained from noisy or under-sampled projection data.

Dong et.al [8] developed an accelerated algorithm for the SIRT algorithm in CT image reconstruction. The proposed SIRT algorithm can handle the image reconstruction problem where projection data is contaminated by Poisson noise and was assigned to solve the linear equation: $Ax = b + n$, where n denotes the statistical noise which is contained in the projection data. The algorithm's efficiency was tested on the reconstruction of a clinical abdominal CT

image. Their results proved that the proposed algorithm had an excellent noise-reducing ability and also a high convergence speed.

Xin et.al [9] implemented simultaneous iteration reconstruction techniques on a GPU with parallel computing languages using compute unified device architecture (CUDA) on four different Nvidia GPU cards (GTX 480, GTX 580, Tesla C2070, and Tesla C2075) in a bid to improve the reconstruction times and lower image noise. The implementation was divided into two steps. The first step was ray tracing for forward-projection and correction and followed by a second step of the back-projection and updating. The SIRT algorithm was implemented by CUDA and run on CPU and GPUs on a Windows workstation which has 8 CPU cores of Intel Xeon 64-bit with 16 GB RAM. The resolution of the reconstruction area was also varied from 8×8 to 256×256. According to their results, the speedup of these algorithms on GPUs varies with resolution. The maximum speedup corresponded to the SIRT algorithm with resolution 128×128 and runs on GTX 480. Overall, the GPU implementations offered significant performance improvement in reconstruction times than CPU.

Simultaneous iterative reconstruction techniques reduce the number of views needed for CT reconstruction. However, the reconstructed images may include ray artefacts (straight lines observed in CT reconstructions as a result of a low number of projection images) which degrade the quality of the data. Bappy and Jeon, [10] implemented a modified simultaneous iterative reconstruction technique for fast, high-quality CT reconstruction (using a GPU to accelerate the calculations) whose aim was to reduce ray artefacts and produce high-quality CT data in fewer iterations than other techniques. For their study, they made use of an aluminum specimen whose projection images were acquired with a micro-CT and reconstructed using the Feldkamp, Davis, and Kress (FDK) algorithm and the SIRT. Their results showed that The FDK reconstruction had sharp edges coupled with a significant amount of ray artefacts. The SIRT reconstruction on the other hand had blurry edges and ray artefacts. The modified method was introduced at this stage, incorporating a geometric non-linear diffusion technique combined with the SIRT reconstruction to minimize the ray artefacts. This technique also converges the algorithms into global minima much faster than other methods, using a minimum number of iterations making it a good choice for micro-CT scanners.

3.10 The ASTRA toolbox

For this research, we make use of the ASTRA Toolbox (All Scales Tomographic Reconstruction Antwerp), a software toolbox that is focused on the reconstruction of three-dimensional datasets [11]. It contains reconstruction algorithms such as the filtered back projection (FBP) and the (SIRT). The toolbox routines work on either a python or MATLAB interface. For fast and efficient implementation of the reconstruction algorithms The ASTRA toolbox can be run on GPU's, but only NVIDIA graphic cards since the algorithms require the CUDA language. Internally, the ASTRA toolbox has 3 layers as shown in figure 3.9. The lower layer provides a platform for implementing algorithm building blocks such as projection and back-projection operators which are GPU accelerated. The C++ middle layer contributes the reconstruction algorithms which make use of these building blocks. The top layer presents an interface that makes it easy to implement these algorithms.

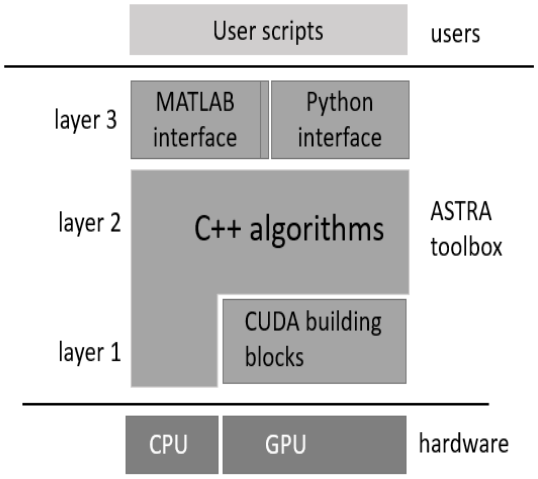

Figure 3.9. Schematic overview of the ASTRA Toolbox design.

The plugin system [12] in the ASTRA toolbox enables the rapid development of GPU accelerated tomography algorithms [12]. The toolbox has a modular design as shown in figure 3.10. These building blocks allow for an efficient implementation of reconstruction methods that can be used to develop new iterative reconstruction methods.

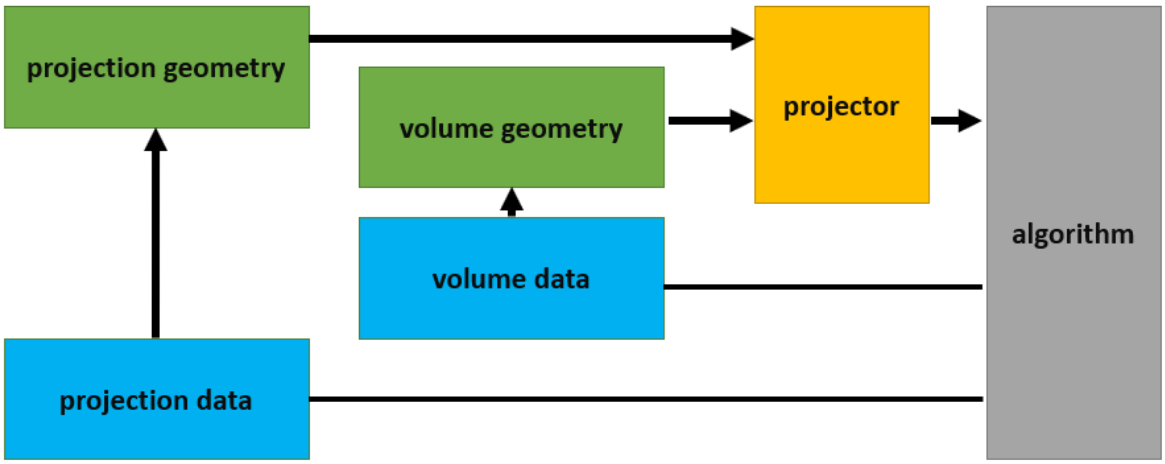

Fig 3.10: The Astra toolbox modules and how they are connected [12].

The projection and volume data objects are linked to their corresponding geometry information (Projection and volume geometry). The geometry information is linked together in a projection algorithm building block which is subsequently used together with the data in the reconstruction algorithm object.

The toolbox also has advanced iterative methods which allow for very flexible scanning in CBCT [12] Palenstijn et.al [11] have also since provided an extension of the ASTRA toolbox with implementations of the SIRT algorithm and back projection that can be distributed over multiple workstations and multiple GPUs to make the processing of large data sets with the ASTRA toolbox feasible.

3.10.1 Projection and volume data

As shown in figure 3.10 above, before the algorithms of the Astra toolbox can be applied to data, that data has to be stored in the ASTRA memory. The volume data module provides a place to store and manage data objects such as reconstruction volumes. The projection data module is responsible for the management and storage of all the datasets for the projection and volume data. The input and output data are supposed to be linked to the geometry that was present when the projections were acquired.

3.10.2 Geometry

The experimental setup of the CT scanner is specified by linking the projection and volume data objects to a corresponding projection and volume geometry. The projection geometry

defines the size of the detector pixels as well as the trajectory of the object around the source and x-ray detector. The volume geometry describes the pixel or voxel grid on which the reconstructed object is represented. For 3D cone-beam geometry, the coordinate system is defined around the reconstruction volume. The center of the reconstruction volume is the origin, and the sides of the voxels in the volume have length 1. All dimensions in the projection geometries are relative to this unit length.

- num_det_rows: number of detector rows in a single projection
- num_det_cols: number of detector columns in a single projection
- angles: projection angles in radians

3.10.2.1 Volume geometry

```
% 3D volume geometry: cuboid voxel grid centered around the origin
vol_geom = astra_create_vol_geom (num_det_rows, num_det_cols, angles );
```

The resulting slice is a square image that has $N_x \times N_x$ pixels and N_x voxels high.

3.10.2.2 Projection geometry

- det_spacing_x: distance between the centers of two horizontally adjacent detector pixels
- det_spacing_y: distance between the centers of two vertically adjacent detector pixels
- det_row_count: number of detector rows in a single projection
- det_col_count: number of detector columns in a single projection
- angles: projection angles in radians
- source_origin: distance between the source and the center of rotation
- origin_det: distance between the center of rotation and the detector array

```
% 3D cone beam projection geometry
proj_geom = astra_create_proj_geom('cone',  det_spacing_x, det_spacing_y,
det_row_count, det_col_count, angles, source_origin, origin_det);
```

3.10.2.3 Creating the reconstruction

Data handling is necessary for the ASTRA toolbox because it does not work with MATLAB double precision matrices directly. An ASTRA data object has to be prepared for the object volume data and linked to the volume geometry. This is identified on the user layer by using a unique identifier (ID).

```
%3D volume data
recon_id = astra_mex_data3d (’create’, ’vol ’ , vol_geom);

After the image data is reconstructed, they are copied back to MATLAB for
writing them into image files and viewing. This is also made possible by
using the unique data object ID.


% retrieve 3D volume data from the ASTRA data object
reconstruction = astra_mex_data3d (’get’, recon_id);
```

The behavior is the same as for the projection data. In this case, however, the sinogram data prepared in a MATLAB double-precision matrix is passed to the creational function of the ASTRA toolbox data object. Since this type of data is only needed for the reconstruction algorithms, there are no retrieve steps needed to be executed.

```
% 3D projection data

sino_id = astra_mex_data3d (’create’, ’-proj3d’, proj_geom , sinogram);
```

3.10.3 Reconstruction algorithms

The reconstruction algorithms are the last and main component of the ASTRA toolbox. On top of the 3D GPU algorithms (SIRT3D_CUDA, FDK_CUDA, BP3D_CUDA) the toolbox also has 2D CPU algorithms such as the FBP and SIRT and 2D GPU algorithms (SIRT_CUDA and FBP_CUDA). In our case the SIRT3D_CUDA is pointed out in the following snippet of the MATLAB code.

```
% 3D SIRT algorithm including a minimum constraint condition
cfg = astra_struct(’SIRT3D_CUDA’);
cfg.ReconstructionDataId = recon_id ;
cfg.option. MinConst raint = minconstr ;
cfg.ProjectionDataId = sino_id ;
alg_id = astra_mex_algorithm (’create’, cfg);
ast ra_mex_algorithm (’ iterate’, alg_id, iters);
```

In the SIRT example, the algorithm has to be linked to the belonging volume and projection data by their corresponding IDs. When all configurations are completed an algorithm ID identifier is generated and then the algorithm is iterated until there is image data in the volume data object of the ASTRA toolbox.

3.11 Application of the ASTRA toolbox to experimental setups

Figure 3.11 shows that the object under investigation has been enlarged onto the detector screen. This is called geometric magnification ***(M)*** in CT and is quantified by the equation 3.1:

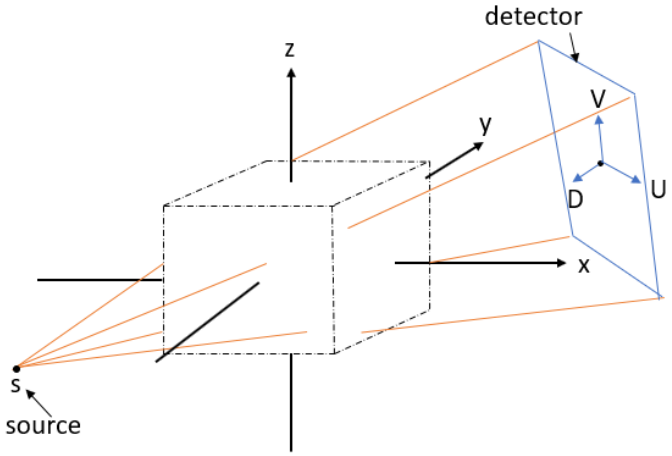

Figure 3.11: Approach to the specification of vector-based cone-beam projection geometry.

To create a projection geometry, the values of d_{so} and d_{od} must be manipulated so as to show that the detector is located on the origin of the coordinate system. The detector is shifted to the origin so that we obtain the equation:

$$\tilde{p}_x := \frac{d_{so}}{d_{so}+d_{od}} p_x = \frac{p_x}{M} \quad \textit{and afterward } \tilde{d}_{od} := 0. \tag{3.8}$$

The value of $\tilde{p}_x$ could also be given in terms of the voxel size V_x which describes the physical dimensions which are covered by one voxel. In the Astra toolbox, all lengths are rescaled so as to achieve the condition $\tilde{p}_x = 1$. Hence this makes the distance measured from the x-ray source to the iso-centre origin become

$$\tilde{d}_{so} := \frac{d_{so}}{\tilde{p}_x} = \frac{\cancel{d_{so}}(d_{so}+d_{od})}{\cancel{d_{so}} p_x} = \frac{d_{sd}}{p_x} \tag{3.9}$$

The flat panel detector used for our 3D cone beam CT scanning has square-shaped detector elements that have dimensions $p_z = p_x$ and hence the 2 manipulations from equations 3.8 and 3.9 suffice.

The ASTRA toolbox has the possibility to describe the projection geometry in a vectorised manner. For cone-beam computed tomography, the projection geometry defines the trajectory of the x-ray source and in vector-based situations, the projection geometry is defined by a vector:

$$V = \epsilon \mathbb{R}^{N_0 \times 12} \tag{3.10}$$

with N_0 showing the number of projection angles considered and each row V_i contains the vectors $V_i = (s_i, d_i, u_i, v_i)$ which are used as row vectors assigned to a projection angle θ_i. As the Astra toolbox expects the detector to be manually placed in the rotation isocentre of the coordinate system, the vectors are assigned to:

% source

$$\widehat{s_\iota} = \begin{bmatrix} \sin(\theta_i)\, \hat{d}_{so} \\ -\cos(\theta_i)\, \hat{d}_{so} \\ 0 \end{bmatrix}^T,$$

% center of detector

$$\hat{d}_{i\,=}\widetilde{d_\iota} = \begin{bmatrix} -\sin(\theta_i)\, \hat{d}_{od} \\ \cos(\theta_i)\, \hat{d}_{od} \\ 0 \end{bmatrix}^T = 0^T$$

% vector from detector pixel (0,0) to (0,1)

$$\widehat{u_\iota} = \begin{bmatrix} cos(\theta_i)\, \hat{p}_x \\ sin(\theta_i)\, \hat{p}_x \\ 0 \end{bmatrix}^T = \begin{bmatrix} cos(\theta_i) \\ sin(\theta_i) \\ 0 \end{bmatrix}^T,$$

% vector from detector pixel (0,0) to (1,0)

$$\widehat{v_i} = \begin{bmatrix} 0 \\ 0 \\ \hat{p}_z \end{bmatrix}^T = \begin{bmatrix} 0 \\ 0 \\ 1 \end{bmatrix}^T \tag{3.11}$$

After creating the vector V above in MATLAB, a vectorised cone beam, projection geometry is generated as:

% 3D vectorised cone beam projection geometry using vector V

proj_geom = astra_create_proj_geom (' cone_vec ' , num_sino , num_det_cols , V) ;

The changes involved in vector V is shown in figure 3.12. The initial position of the CBCT scanning scenario is indicated by d_1,v_1, *and* u_1**.** At a given projection angle $\boldsymbol{\theta_i}$**,** the scanning position is marked by the vectors d_i,v_i, *and* u_i. This shows that the vectors *s, d* and *u* vary under trigonometric functions and are dependent upon the projection angle $\boldsymbol{\theta_i}$ which is reflected in equation 3.11. However, the vector v which points out of the paper plane does not vary as the projection angles $\boldsymbol{\theta_i}$ increase. Hence starting at an arbitrary d_i,v_i, *and* u_i, and shifting the detector to the origin as shown in equation 3.8 and then standardizing as shown in equation 3.9, we produce the input vectors in equation 3.4 for a vectorised projection geometry in the ASTRA toolbox.

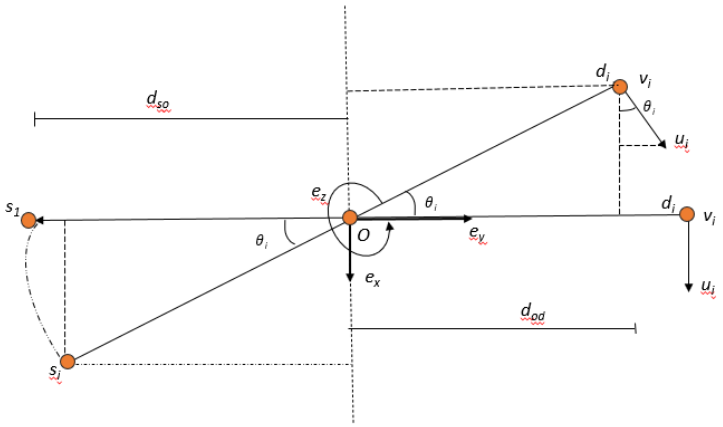

Figure 3.12: An auxiliary illustration for vector-based image reconstruction.

3.12 Sinograms

Sinogram images in the ASTRA toolbox are made in a process of the re-arrangement of projection data which does not comprise any pixel value editing. In a given projection data,

each projection image has the dimensions $N_z \times N_x$ which are equal to the flat panel detector's resolution. In a cone beam CT scanning scenario, the entirety of projection images counts N_0 single images, where N_0 also represents the number of projection angles of the measuring process. We fix a single row on the detector which has N_x pixel values and by doing this we track all the projection angles N_0 for grey values of this trend. This means that every sinogram has $N_0 \times N_x$ pixel values which are N_z large, with N_z being the number of rows on the flat panel detector. Figure 3.13 shows a sinogram obtained from a CT scan of a palaeontological specimen (the tooth of an *anteosaurcus magnificus*) for $N_0 = 3141$ projection angles. When the projection data of the specimen is converted to a sinogram, the sinogram itself is observed as a sinusoidal wave along the image rows serving as an ordinate.



Figure 3.13: A sinogram from CT data

The reason for the rearrangement of projection data to sinogram data is as follows: The sinogram which corresponds to a detector row with the dimensions $N_x \times N_x$ contains all the data which is required (by the chosen reconstruction algorithm) for a slice to be reconstructed from the ASTRA toolbox.

References: Chapter 3

1. Ritman, E.L., 2011. Current status of developments and applications of micro-CT. *Annual review of biomedical engineering*, *13*, pp.531-552.
2. Zhou, F., Li, Z., Lan, W., Wang, Q., Ding, L. and Jin, Z., 2020. Halide Perovskite, a Potential Scintillator for X-Ray Detection. *Small Methods*, *4*(10), p.2000506.
3. Carlson, W.D., Denison, C. and Ketcham, R.A., 2000. High-resolution x-ray computed tomography as a tool for visualization and quantitative analysis of igneous textures in three dimensions. *Visual Geosciences*, *4*(3), pp.1-14.
4. Chang, Z., Ye, D.H., Srivastava, S., Thibault, J.B., Sauer, K. and Bouman, C., 2018. Prior-guided metal artifact reduction for iterative x-ray computed tomography. *IEEE transactions on medical imaging*, *38*(6), pp.1532-1542.
5. Hunt, P.K., Engler, P. and Bajsarowicz, C., 1988. Computed tomography as a core analysis tool: Applications, instrument evaluation, and image improvement techniques. *Journal of Petroleum Technology*, *40*(09), pp.1203-1210.
6. Rashid, S., Lee, S.Y. and Hasan, M.K., 2012. An improved method for the removal of ring artifacts in high resolution CT imaging. *EURASIP Journal on Advances in Signal Processing*, *2012*(1), pp.1-18
7. Che, S., Boyer, M., Meng, J., Tarjan, D., Sheaffer, J.W. and Skadron, K., 2008. A performance study of general-purpose applications on graphics processors using CUDA. *Journal of parallel and distributed computing*, *68*(10), pp.1370-1380.
8. Dong, J., Kudo, H. and Kim, Y., 2020, January. Accelerated algorithm for the classical SIRT method in CT image reconstruction. In *Proceedings of the 5th International Conference on Multimedia and Image Processing* (pp. 49-55).
9. Xin, J., Bardel, C., Udpa, L. and Udpa, S., 2013, January. GPU implementation of simultaneous iterative reconstruction techniques for computed tomography. In *AIP Conference Proceedings* (Vol. 1511, No. 1, pp. 777-784). American Institute of Physics.
10. Bappy, D.M. and Jeon, I., 2017. Modified simultaneous iterative reconstruction technique for fast, high-quality CT reconstruction. *IET Image Processing*, *11*(9), pp.701-708.
11. Palenstijn, W.J., Bédorf, J. and Batenburg, K.J., 2015. A distributed SIRT implementation for the ASTRA toolbox. *Proc. Fully Three-Dimensional Image Reconstruct. Radiol. Nucl. Med*, pp.166-169.
12. Van Aarle, W., Palenstijn, W.J., Cant, J., Janssens, E., Bleichrodt, F., Dabravolski, A., De Beenhouwer, J., Batenburg, K.J. and Sijbers, J., 2016. Fast and flexible x-ray tomography using the ASTRA toolbox. *Optics express*, *24*(22), pp.25129-25147.

4 Pre-processing of projection data

4.1 Introduction

As stated in Chapter 1, the CT scanner at our facility uses the filtered back-projection (FBP) algorithm. Although this method is efficient and involves simple calculations, the filter functions used with this model are susceptible to image noise and streak artefacts. In addition to this, there are large discontinuities in detector measurements that are created when the metal edges are amplified by the FBP [1]. Hence, this work seeks to investigate the effects of adding an image processing step before performing computed tomography reconstructions. The goal is to acquire projections with the Inspect-X software and use ImageJ, a flexible image-processing package, an open-source program developed by the National Institutes for Health (NIH) [2], to carry out image filtering at the stage of CT reconstruction using convolution filters which are explained briefly in the next section. The foreseen benefit of performing image processing on projections before reconstruction is that in cases where information about the sample is already available, one may be able to implement the necessary adjustments at this stage. The aim is to reduce the effects of metallic inclusions in the data and hence improve the image quality. ImageJ can read a variety of image file formats including TIFFs used for this work [2]. The tiff image files are grayscale and 16-bit images with a size of 2 000 × 2 000 pixels.

4.2 Convolution Filtering

Convolution filtering is a process of adding pixel values (weighted by a kernel) of an image to its local neighbours [3]. A kernel is a matrix whose centre corresponds to the source pixel and the other matrix elements correspond to neighbouring pixels. The destination pixel is calculated by multiplying each source pixel by its corresponding kernel coefficient and adding the results. To illustrate this process, we use two 3×3 matrices shown in equation 4.1. The 1st matrix represents a filter kernel, and the 2nd matrix represents an image slice decomposed into its pixel values [3]. The kernel is overlapped with the image matrix, the overlapping indices are multiplied and added, to replace the value of the central element. The central element of the resulting image (co-ordinates [2, 2]) would be a weighted combination of all the entries of the image matrix, with weights given by the kernel:

$$\left(\begin{bmatrix} a & b & c \\ d & e & f \\ g & h & i \end{bmatrix} \times \begin{bmatrix} 1 & 2 & 3 \\ 4 & 5 & 6 \\ 7 & 8 & 9 \end{bmatrix}\right) [2, 2] = 2\,(i \times 1) + (\mathrm{h} \times 2) + (\mathrm{g} \times 3) + (f \times 4) + (e \times 5) +$$

$$(d \times 6) + (\mathrm{c} \times 7) + (\mathrm{b} \times 8) + (\mathrm{a} \times 9) \qquad (4.1)$$

The other entries would be similarly weighted with the centre of the kernel always positioned on each of the boundary points of the image so as to compute the weighted sum.

4.3 Experimental procedure

We have acquired projections with a micro-computed tomography scanner and carried out image processing functions for the improvement of the quality of the data output using a paleontological specimen (the tooth of an *anteosaurcus magnificus*) with a significant amount of iron inclusions which cause bright and dark streak artefacts. The acquisition was carried out using x-ray photons generated at 110 kV and at a resolution of 32 µm. Metal filters of Copper with a thickness of 1.2 mm were used to cut out the low energy component of the beam in order to avoid saturating the detector. The optimum number of 3141 projections were acquired whilst rotating the sample through 360° as determined by the relation explained in section 3.6.4 so that we do not introduce sampling errors. We have applied several filters to alter the projections before reconstruction as shown in figure 4.1:



Figure 4.1: Tooth of an *anteosaurcus magnificus* used as the test specimen.

Figure 4.2 shows a cross-section of the specimen with streak artefacts due to the effect of metallic inclusions. This data was obtained and used to observe the effects of applying the different filters.

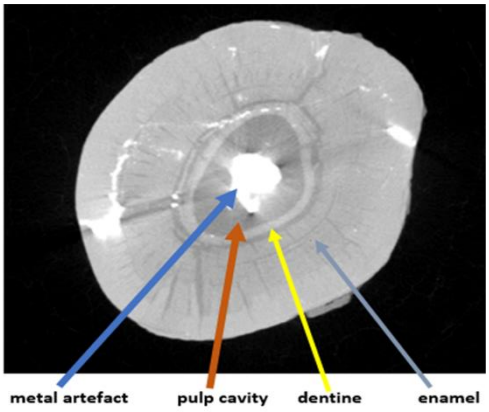

Figure 4.2: A cross-sectional view of the tooth of an *anteosaurcus magnificus*.

As observed in figure 4.2, the specimen is infested by metallic inclusions which appear bright. This causes bright and dark streak artefacts which can be observed around the slice. In the next section, we describe the four different filters which are used independently in this work for the CT data enhancement.

4.3.1 Mean Filter

Mean filtering is a method of smoothing images by reducing the amount of intensity variation between one pixel and the next [4]. In ImageJ, the mean filter is implemented as a convolution operation with equal weights in the convolution mask. This process works by replacing each pixel value in an image with the average pixel value of its neighbours and itself [4]. For a total number of pixels M in a given neighbourhood N. A noisy image *f* with matrix indices *[k, l]* is denoised to produce an image *h* which matrix indices [*i, j*] as given by equation 2,

$$h\,[i,j] = \frac{1}{M}\sum_{(k,l)\epsilon N} f\,[k,l]. \qquad (4.2)$$

M is the total number of pixels in a given neighbourhood N. The size of the neighbourhood is described in terms of a radius. A radius of 1 pixel describes a 3×3 neighbourhood and a radius of 2 pixels describes a 5×5 pixel neighbourhood. The mean filter was applied onto the projections with 2 different values for the radius (1and 2) and the results shown in figure 4.3 were compared to the original scans for the slice chosen as a reference after reconstruction.

(a) 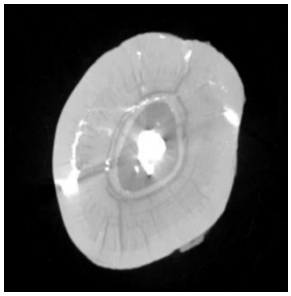 (b) 

Figure 4.3: Shows a cross-sectional view of the specimen after applying a mean filter of radius 1 pixel (a) and 2 pixels(b)

As can be observed in each of these slices, the mean filter significantly reduced the streak artefacts by replacing image pixels with a mean of their surroundings. On implementation of the 5×5 mean filter kernel, the streak artefacts become less and less visible and the image undergoes further smoothing thereby significantly reducing the image noise.

4.3.2 Median Filter

The median filter is also used to reduce noise in an image. In a similar way to the mean filter, the median filter considers each pixel in the image and in turn, replaces the pixel values in a specific range with their median of those values [5]. The output of the median filter is given by the expression,

$$g(x,y) = med\{f(x-i, y-j), i, j \epsilon W. \quad (4.3)$$

In this equation, $f(x,y)$ represents the original image, and $g(x,y)$ is the output image after the image has been filtered with a kernel mask represented by W. The size of this mask is in terms of $n \times n$ where n is an odd number such as 3×3 for a radius of 1 pixel and 5×5 for a radius of 2 pixels. The median filter is considered to be non-linear, hence the noise variance under normal distribution for an image with zero mean noise is given by,

$$\sigma_{med}^2 = \frac{1}{4nf^2(\overline{n})} \approx \frac{\sigma_i^2}{n+\frac{\pi}{2}-1} \times \frac{\pi}{2}, \quad (4.4)$$

where the variance σ_i^2 represents the input noise power, *n* represents the size of the filter kernel and the function $f(\overline{n})$ represents the noise density. As is with the mean filter, the median filter was also applied onto the projections with 2 different values for the radius (1and 2), and the results shown in figure 4.4 were compared to the original scans for the slice chosen as a reference after reconstruction.

(a) 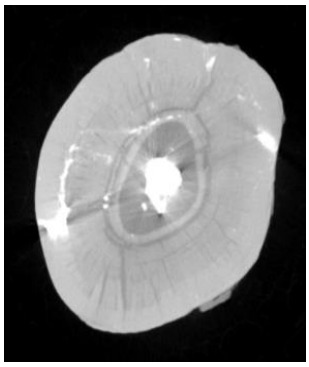 (b) 

Figure 4.4**:** Shows a cross-sectional view of the specimen after applying a median filter of radius1 pixel (a) and 2 pixels (b).

With the median filter of radius 1 pixel, any pixel value which is not representative of the surrounding pixels is replaced by the median value of a 3×3 square neighbourhood. The filter (3 x 3 kernel) considerably enhances edges in an image. However, the streak artefacts are still significantly visible as the filter does not deal with speckle noise. As the radius of the median filter is increased to 2 pixels (5×5 filter kernel), the image undergoes further edge enhancement. However, since the median filter preserves the edges of an image but does not deal with noise, the streak artefacts are more visible.

4.3.3 Gaussian smoothing

The Gaussian filter is a 2D convolution operator which smoothens CT data and reduces noise by blurring. This filter uses a kernel that has the shape of a bell-shaped hump which outputs a weighted average towards the value of the central pixels. A Gaussian distribution with a mean of zero has the form;

$$G(x) = \frac{1}{\sqrt{2\pi}\sigma} e^{-\frac{x^2+y^2}{2\sigma^2}} \quad (4.5)$$

where σ represents the standard deviation of the Gaussian distribution with coordinates x and y. The degree of smoothing is determined by the standard deviation of the Gaussian. Hence larger standard deviation Gaussians will require larger convolution kernels to be represented accurately. The filter assumes that out-of-image pixels have a value equal to the nearest edge pixel and as such, it provides gentler smoothing and preserves edges [6]. The Gaussian blur

filter was applied to the CT data with sigma (radius) 1 and 2 pixels and the results shown in figure 4.5 were compared with those obtained from the other filters used.

(a) 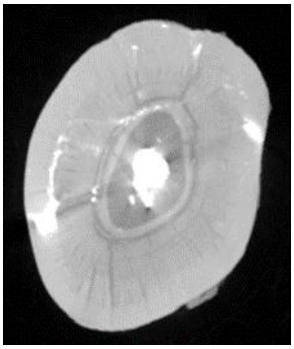 (b) 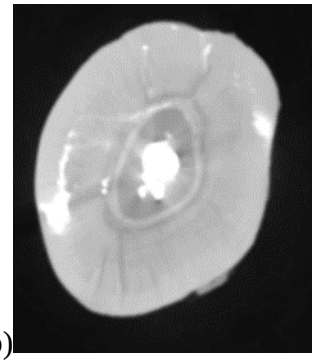

Figure 4.5: Shows a cross-sectional view of the specimen after applying a gaussian filter of sigma radius 1(a) and 2 (b).

The Gaussian smoothing filter also successfully reduces the noise in the image. As shown above, when the sigma radius is increased to 2 pixels, The image noise is greatly reduced, and the streak artefacts become less and less visible.

4.3.4 Unsharp filter

The unsharp filter is a sharpening operator which enhances edges and other high-frequency components in an image [7]. The algorithm of unsharp masking involves subtracting a smoothed version of an image from the original image and rescaling the image to obtain the same contrast of large (low frequency) structures as in the input image. This is equivalent to adding a high pass filtered image and thus sharpens the image. The unsharp masking is a convolution operation that is performed on an image whose kernel mask is that of a 2D Gaussian function *g (x, y)* and is derived from equation 4.5 as follows:

$$g(x,y) = G\ (X,\ Y) = \frac{1}{\sqrt{2\pi\sigma}} e^{-\frac{x^2+y^2}{2\sigma^2}} \qquad (4.6)$$

4.3.4.1 Gaussian Radius

This is the standard deviation (σ blur radius) of the Gaussian blur that is subtracted. Increasing the Gaussian blur radius will increase the contrast.

4.3.4.2 Mask Weight

Determines the strength of filtering, whereby mask weight = 1 would be an infinite weight of the high pass filtered image that is added. Increasing the mask weight value will provide additional edge enhancement.

The size of the kernel mask is an important parameter as it defines the range of frequencies to which the Gaussian filter acts and removes. In this case, it is defined by the standard deviation of the Gaussian distribution. The unsharp mask (A blurred image produced in the filtering process) is subtracted from the original image according to the equation:

$$f(x,y) = \frac{c}{2c-1} I\ (x,y) - \frac{1-c}{2c-1} U\ (x,y) \qquad (4.7)$$

For an image pixel at the coordinates *(x, y)* the function $f(x,y)$ is a representation of the brightness value of the respective pixel in the image. The function $I\ (x,y)$ is a representation of the pixel brightness in the input image and *U (x, y)* in the blurred (unsharp mask) image. The constant *c* found in the difference equation acts as a control to the weighting of the blurred and the original image. As shown by equation 4.7, the unsharp mask filter works by removing a weighted form of the unsharp mask from the input(original) image. An increase in the mask weight value would provide an additional edge enhancement. What this operation does is an enhancement of high-frequency spatial information of the image at the expense of low-frequency spatial detail. For this work, the unsharp mask filter was applied to the projection with sigma (radius) 1 and 2 pixels with the mask weight kept constant at 0.60 and the results shown in figure 4.6 were compared with those obtained from the other filters used.

(a) 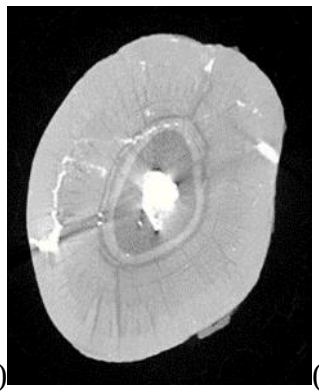 (b) 

Figure 4.6: Shows a cross-sectional view of the specimen after applying an unsharp mask filter of sigma radius 1 pixel (a) and 2 pixels (b) with a mask weight of 0.60.

As stated before, the Gaussian filter alone will blur edges and reduce contrast. The unsharp mask filter of sigma radius of 1 pixel enhanced the edges in the image and also reduces the streak artefacts significantly. However, this filter in nature enhances other high-frequency components in an image, and as such, the noise is also accentuated. As the radius of the filter is increased from 1 to 2 pixels, the edges are further enhanced and become more visible since this filter increases the pixels' contrast in the specimen.

4.4 A quantitative approach to image quality evaluation

The objective of this work is to use a quantitative measure that gives an impression of image quality by considering quality-reducing effects (streak artefacts and noise). The image quality measurement proposed in this work is calculated based on a grey value histogram and is a measure for the degree of separation of material classes in the analyzed data. Figure 4.7 shows a histogram of the same tooth specimen (when no filter has been applied).

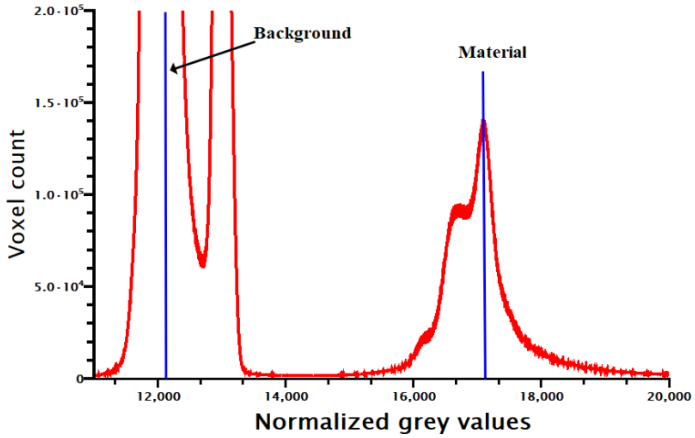

Figure 4.7: Histogram showing the grey values of the tooth of an *anteosaurcus magnificus* obtained from CT and then reconstruction using CT Pro 3D.

The histogram contains a class labelled material which in this case represents the tooth and another one for air (background). From the histogram data, the high-density material which is more absorbing is represented with higher grey values and on the right-hand side of the histogram. On the other hand, air particles and low-density objects in the data are represented with lower grey values and are towards the left-hand side of the histogram. The distribution of this histogram shows cumulated information of the image which in turn gives an impression of the quality of CT data. The width of the measurement for a class is regarded as a combined measure of the strength of noise and artefacts in the data [9].

4.4.1 Image quality

Quantitative data analysis was performed using VGStudio Max 3.5 software by performing a grey value analysis. The tooth of an *anteosaurcus magnificus* was used as the test specimen and the image quality metric proposed is defined as follows.

$$Q = \frac{|\mu_2 - \mu_1|}{\sqrt{\delta_1^2 + \delta_2^2}} \tag{4.8}$$

Where μ is the mean grey value and δ is the standard deviation of the histogram distribution for material (2) and air (1) respectively [9].

4.4.2 Standard deviation

The standard deviation in this case is defined as a measure of the amount of dispersion for the grey values. A low standard deviation is an indication that the values tend to be close to the mean which in this case indicates low image noise [10]**.**

Let μ be the expected value (mean of the grey values) X with density function $f(x)$:

$$\mu \equiv E[X] = \int_{-\infty}^{+\infty} x\, f(x)dx, \tag{4.9}$$

the standard deviation σ of X is defined as:

$$\sigma \equiv \sqrt{E[(X - \mu)]^2} = \int_{-\infty}^{+\infty} (x-\mu)^2 f(x)dx \tag{4.10}$$

which can be shown to be equal to [10]:

$$\sqrt{E[X^2] - E[X]^2} \tag{4.11}$$

And hence the standard deviation is the square root of the variance of the mean of the grey values *(X)*.

4.4.3 Image noise

Noise is influenced by factors relating to the scan settings, the x-ray detector and the reconstruction algorithms which are used to reconstruct the data. By increasing the source current, one increases the number of photons detected and this reduces the noise in CT data. Photons with a higher energy have a greater probability of penetrating through an object. This will increase the number of detected photons and at the same time reducing the noise in CT data. One can also increase the exposure time which will increase the number of detected photons per pixel and reduce the noise. Quantum noise is dependent on the number of detected

photons and hence it is affected by the detector characteristics. Increasing the pixel size will lower the image noise. The number of projections taken at any given angle can be averaged to reduce image noise. This is based on the fact that shot noise is randomly distributed across the detector pixels and hence one can reduce these random fluctuations by means of averaging similar images. Implementation of iterative reconstruction algorithms also reduces noise in CT data as shall be discussed in chapter 5.

The direct grey value analysis obtained using the software VGStudio MAX contains values of the maximum and the minimum grey values as well as the mean and the standard deviation of the grey values. This eliminates an additional step of processing (obtaining the values from a histogram output). To quantify the image improvement as a function of the different filters applied to the data, a measure was needed to give a representation of the noise in the reconstruction. A full-width-half-maximum (FWHM) of the air peak was selected. In a grey value distribution, the full width at half maximum (FWHM) is the difference between the two values of the grey values at which the voxel count is equal to half of its maximum value. The width of a spectrum curve is measured between those points on the y-axis (figure 4.8) which are half the maximum amplitude [11].

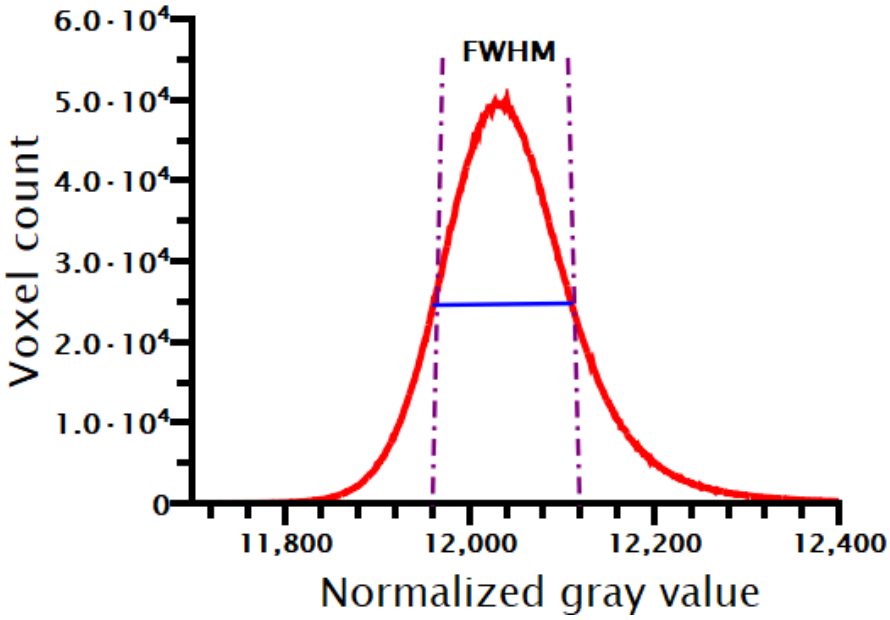

Figure 4.8: Full width at half maximum for the *anteosaurcus magnificus* when no filter was applied.

If the considered function is the density of a normal distribution of the form:

$$f(x)=\frac{1}{\delta\sqrt{2\pi}}e^{\left[\frac{(x-x_0)^2}{2\delta^2}\right]} \qquad (4.12)$$

where σ is the standard deviation and x_0 is the expected value. The FWHM for a Gaussian distribution is obtained by finding its half-maximum points. The constant scaling factor can be ignored and hence we must solve:

$$e^{\left[\frac{(x-x_0)^2}{2\delta^2}\right]}=\frac{1}{2}\,f\,(x_{max}).$$

$f\,(x_{max})$ however occurs at $x_{max} = x_o$

and hence $e^{\left[\frac{(x-x_0)^2}{2\delta^2}\right]}=\frac{1}{2}\,f\,(x_o)=\frac{1}{2}$

$$e^{\left[\frac{(x-x_0)^2}{2\delta^2}\right]}=2^{-1}$$

$$\left[\frac{(x-x_0)^2}{2\delta^2}\right]=\ln 2$$

$$(x-x_0)^2=2\delta^2\ln 2$$

$$x=\pm\,\delta\,2\sqrt{2ln2}\delta+x_o \qquad (4.13)$$

The FWHM is therefore given by:

$$FWHM=2\sqrt{2ln2}\delta \qquad (4.14)$$

The FWHM method is measured from the standard deviation δ for each histogram and used to quantify the image noise in computed tomography data.

For palaeontological specimens, obtaining an image with reduced noise is important as it allows one to accurately segment the regions of interest inside the fossil faster [8]. The background noise in the image was measured for all the filters applied to the CT data and was measured from a uniform region of interest *(x=1332.69, y =904.57, z =707.00)* as the standard deviation of the mean grey values obtained from the volume of the region of interest shown by the green square in figure 4.9.

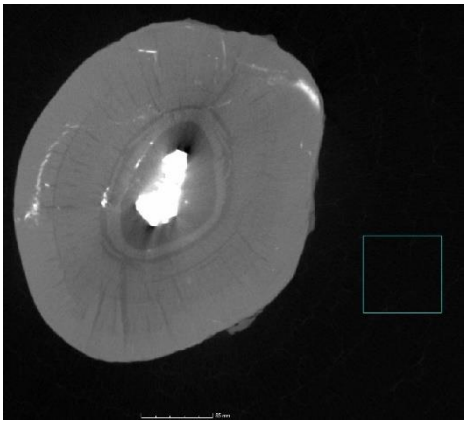

Figure 4. 9: Region of interest to measure the background noise in the image.

4.5 Image quality results

The results of the image qualities obtained by using different filters are shown in figure 4.10. The Q factor was calculated from the grey value distributions of the air and the tooth using equation 4.8

gf = Gaussian filter

mf = mean filter

md = median filter

um = unsharp mask filter

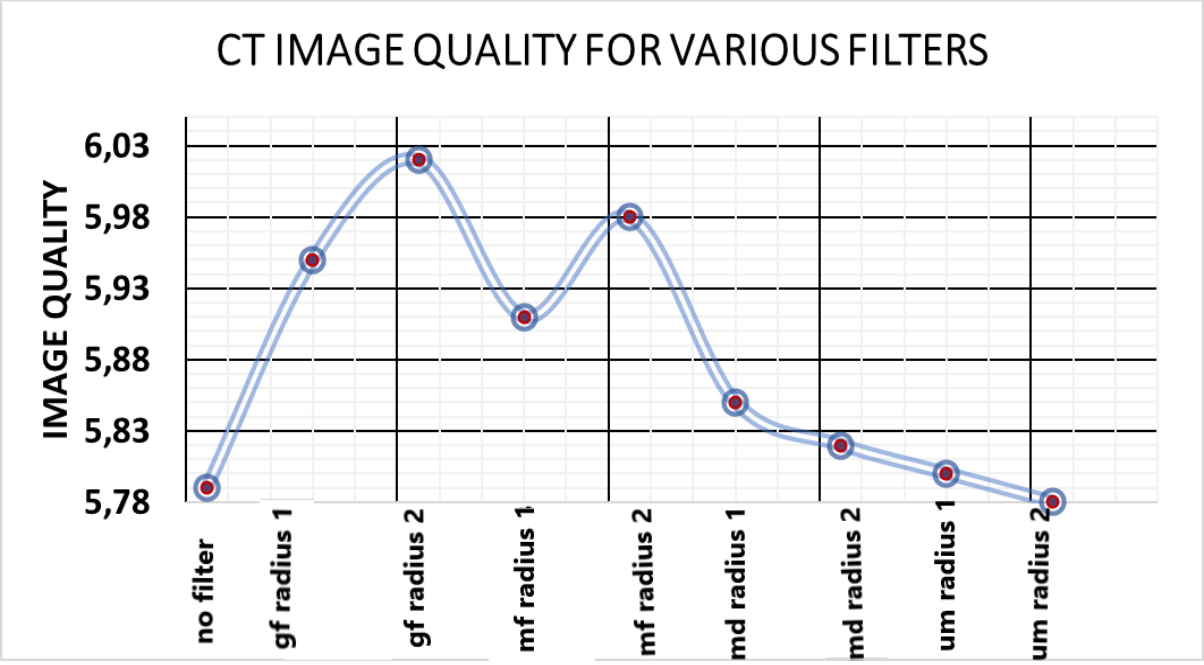

Figure 4.10: The effect of varying filtering options on the image quality.

The width of the peaks in the reconstructed data set was studied as a function of the various filters applied to the projections to reduce the noise and was calculated using equation 4.14. The results are shown in figure 4.11.

gf = Gaussian filter

mf = mean filter

md = median filter

um = unsharp mask filter

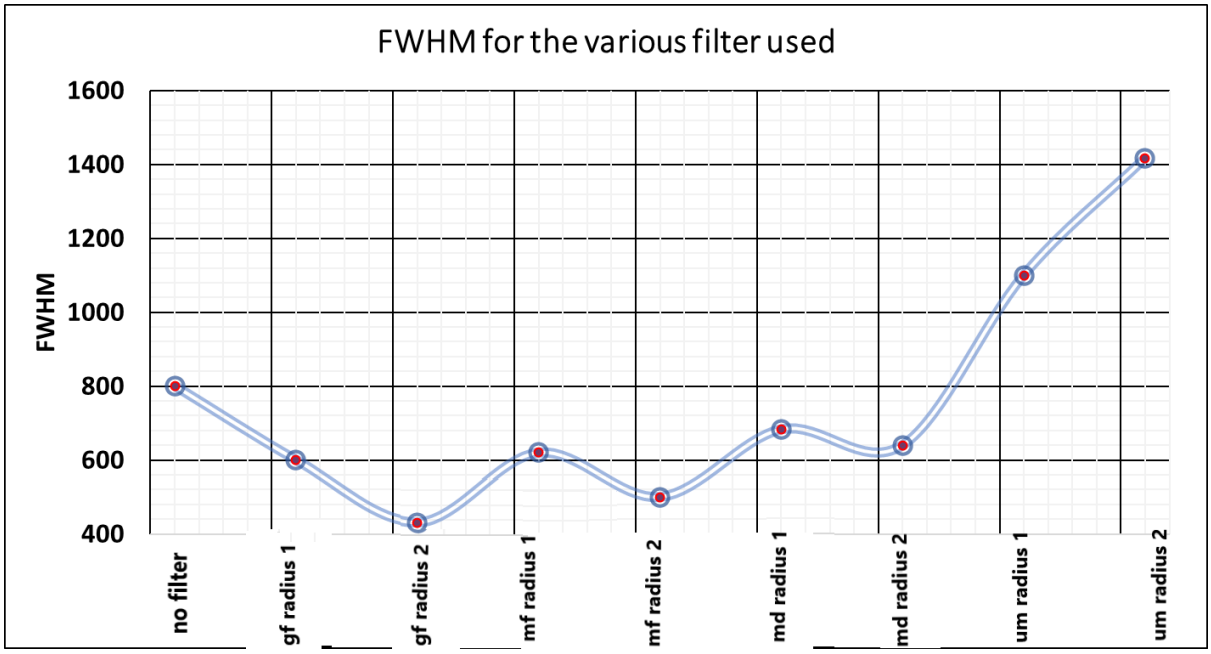

Figure 4.11: Background noise measured as the FWHM.

4.5.1 No filter

The effects of filtering CT data at the reconstruction stage were investigated quantitatively. As expected, the use of most of the filters improves the image quality and reduces streak artefacts. Using equation 4.8, the image quality Q_1 when no filter was applied to the projections was calculated to be 5.79. The FWHM used to measure the image noise gives a measured full width half value (FWHV) of 800 at this point.

4.5.2 Gaussian filter

The use of the Gaussian filter (radius =1 pixel) on the projections resulted in the image quality Q_1 increasing from 5.79 to 5.95. The increase in the image quality is attributed to the Gaussian smoothing which is used to remove Gaussian (random) noise from the image and hence the FWHV to 600. While removing the noise also reduces the streak artefacts as well as preserves edges in the data. As the sigma radius is increased, the image quality is further increased to 6.02 due to the increased smoothing of the data. The FWHV further drops down to 433. However, as the radius is further increased to 2 pixels, the contrast is reduced due to excessive smoothing of the images and as such, a low sigma radius filter would ensure one reduces the noise and streak artefacts at the same time ensuring that not as much contrast is lost.

4.5.3 Mean filter

The use of the mean filter (3×3) also sees a significant improvement in the image quality to 5.91. With the mean filter, each new pixel now depends on the average of the values for example in the pixel region. The measured FWHV is 620 and hence the image quality increases. The 5×5 mean filter kernel further smoothens the image reducing the FWHV to 500 and hence the image quality increases to 5.98. However, it results in loss of edge information and as such, a 3×3 filter would be best used in this case.

4.5.4 Median Filter

The median filter (3×3) does not create new pixel values when the filter straddles an edge. Hence the filter also significantly increases the image quality to 5.85 with a FWHV of 683. As the filter kernel size is increased to a (5×5) the image quality is reduced to 5.82. And hence as the filter size is increased the streak artefacts are enhanced significantly, which accounts for the slight loss in image quality.

4.5.5 Unsharp mask filter

The unsharp filter is a sharpening operator, which subtracts an unsharp version of an image from the original image. The mask with a radius of 1 pixel was successful in enhancing the image edges and slightly increasing the image quality to 5.8. However, the results show that it

produces a poor result in the presence of noise as the FWHV was accentuated highly to 1100. When the filter kernel with a sigma radius of 2 pixels was used, the image quality was reduced quality to 5.78 and the FWHV also further increased to 1416. These results show that although the unsharp mask is very essential in increasing edge sharpness, it also increases noise in the CT data.

4.6 Conclusions

This work has demonstrated an approach to image quality measurement applicable to micro-CT. Firstly, we investigated the use of pre-processing filtering qualitatively for the different filters used (see figures 4.3- 4.6). The results in figure 4.3(a) show that applying the mean filter smoothens the CT data thereby reducing noise and streak artefacts. When the filter radius is increased to 2 in figure 4.3(b), the image undergoes further smoothing which significantly reduces the streak artefacts. This filter smoothens data by replacing each pixel value in an image with the average pixel value of its neighbours and itself and hence the larger the filter kernel the greater the smoothening. In figure 4.4 (a and b), the use of the median filter enhances edges in the CT data. This filter however does not deal with speckle noise and hence the noise together with streak artefacts are still significantly visible. When the radius of the median filter is increased to 2, the image edges are further enhanced whilst the noise in and streak artefacts become more visible. The use of the Gaussian filter as observed in figure 4.5 (a and b) smoothens the image thereby significantly reducing noise and streak artefacts in the CT data. The degree of smoothing is determined by the radius of the Gaussian and hence a larger radius will result in more image smoothing. In figure 4.6 (a and b), the unsharp mask filter enhances edges and other high-frequency components in an image which includes the noise which is significantly visible in the data. The algorithm of unsharp masking involves subtracting a smoothed version of an image from the original image and rescaling the image to obtain the same contrast of large (low frequency) structures as in the input image. Hence, as the radius of the unsharp mask filter is increased in figure the noise and streak artefacts are also increased.

A quantitative image quality evaluation was also performed using the Q value measurement in (equation 4.8) and the FWHM method (see equation 4.14). The Gaussian filter was found to produce data with the highest image quality (figure 4.10) as well as data with the least noise (figure 4.11). On the other hand, the unsharp mask filter produces images with the lowest image quality (figure 4.10) and the highest noise (figure 4.11). The mean filter and the median also significantly improve the image quality as well as reduce the noise accordingly. According to

these results, the use of a filter for pre-processing of projections results in an improvement of CT image quality, either by smoothening of the projections for noise reduction as seen by the Gaussian and the mean filter or by edge enhancement as seen by the median and the unsharp mask filter. Excessive use of image smoothening (Gaussian blur radius 2) will cause loss of image sharpness and hence its use should be limited, especially when fine features are of interest.

References: Chapter 4

1. Gonzalez, R. C. and Woods, R. E. 2002. *Digital Image Processing 2nd Ed*, Prentice-Hall, Upper Saddle River, New Jersey.
2. Girish V and Vijayalakshmi A 2004. *Affordable image analysis using NIH Image/ImageJ*. Indian J Cancer. 41 (1): 47.
3. Seletchi E. D. and Duliu O. G. 2006. *Image processing and data analysis in computed tomography*. Romanian Journal of Physics.
4. Jain A. 1989. *Fundamentals of Digital Image Processing*, Prentice-Hall, Chap. 7.
5. Gammon S. T, Leevy W. M, Gross S, Gokel G.W, and Piwnica-Worms D. 2006. *Spectral unmixing of multicoloured bioluminescence emitted from heterogeneous biological sources*. Anal Chem, 78(5):1520–7.
6. Getreuer P. 2013. *A Survey of Gaussian Convolution Algorithms*. Image Processing on Line. 3: 286–310.
7. Schalkoff *R. 1989. Digital Image Processing and Computer Vision*. John Wiley & Sons, Chap. 4.
8. Tshibalanganda, M., du Plessis, A., Le Roux, S.G., Taylor, W.L., Smith, R.M. and Browning, C., 2019. *Systematic experiments to quantitatively assess image quality for CT scans of a Karoo tetrapod fossil*.
9. Reiter, M., Weiß, D., Gusenbauer, C., Erler, M., Kuhn, C., Kasperl, S. and Kastner, J., 2014. *Evaluation of a histogram-based image quality measure for X-ray computed tomography*. Proceedings of iCT Wels, 2014.
10. Bland, J.M. and Altman, D.G., 1996. *Statistics notes: measurement error proportional to the mean. Bmj*, 313(7049), p.106.
11. Cho, Y.H., Seo, J.B., Kim, N., Lee, H.J., Hwang, H.J., Kim, E.Y. and Oh, S.Y., 2015. *Comparison of a new integral-based half-band method for CT measurement of peripheral airways in COPD with a conventional full-width half-maximum method using both phantom and clinical CT images*. Journal of computer-assisted tomography, 39(3), pp.428-436.

5 Reconstruction with the ASTRA toolbox

5.1 Introduction

The design of the ASTRA toolbox is summarized in section 3.9. In this chapter, we will go on and present the main steps to perform the reconstruction which include flat-field corrections as well as centre of rotation corrections. We also describe the approach used to perform CT data reconstruction as well the results obtained.

5.2 Flat field correction with the ASTRA toolbox

The Astra toolbox offers a wide range of functionalities and reconstruction techniques to the user. However, one has to provide additional pre and post-processing steps so as to obtain the desired reconstruction images. This applies to the image processing from raw projection data to normalized ones as well as center of rotation misalignments which are done using the vectorized projection geometries in the ASTRA toolbox routines.

5.2.1 Normalization

This is a pre-processing step also known as the flat field correction which is used to correct for the variations of the x-ray source intensity and the detector sensitivity. There are two main effects to take into consideration which are the dark current of the detector as well as flat fields.

5.2.2 Dark current

The dark current also known as leakage current is an electronic phenomenon that causes the detector pixels to report values when the x-ray source is turned off. The relationship between the input (actual x-ray intensity) and the output (detector sensitivity) can be written as

$$y = gx + b, \tag{5.1}$$

where x is the input, y is the output, g is the detector gain and b is the dark current. For one to measure the dark current, the x-ray source has to be turned off which implies that $x = 0$. Taking the dark frames as d, the equation for the imaging system becomes

$$d = gx + b \tag{5.2}$$

Setting x to 0 results in the equation

$$d = b \qquad (5.3)$$

Which implies that the dark frames on the detector provide the contribution of the dark current.

5.2.3 Flatfields

The intensity variations in the detector are not the same for each pixel. This is due to imperfections of the detector panel as well as effects such as using an inhomogeneous x-ray source. Hence one needs to turn on the x-ray source and obtain an image without any object placed in the field of view. In an ideal scenario, this process would produce a homogenous image, however due to the imperfections mentioned, it does not but the resulting image is a representation of exactly how "unflat" the x-ray imaging system is. To demonstrate the flat field correction, we set x which is our input to a constant value say $x = 1$. When we obtain the flat fields, the imaging system equation becomes

$$f = gx + b. \qquad (5.4)$$

However, since $x = 1$, the equation becomes

$$f = g + b\ , \qquad (5.5)$$

which results in

$$g = f - b\ . \qquad (5.6)$$

If we substitute this equation into $y = gx + b$ and use the fact that $d = b$, we get the equation

$$y = (f - d)x + d \qquad (5.7)$$

As the equation which describes the imaging system. If we are to rewrite this in terms of the functions of known values d and f, the original input intensity x is then computed from the measured pixel value y through the use of the equation,

$$x = \frac{y-d}{f-d} \qquad (5.8)$$

The equipment used in this report collects flat field and dark field images at the beginning and then applies the correction to all projections before they are saved. Reconstruction of the 3D image is then carried out using these projections. With normalized images, the projection data is rescaled relative to the relative surrounding medium to resolve any defects coming from distortions in the x-ray path. The image data obtained is in the double-precision matrix and can

then be written to image files of the desired output as in our case 16-bit TIFF using MATLAB standard routines. The following code snippet is used for normalization of the data in the ASTRA toolbox.

```
IMG = projections;

%IMG = im2double(projections,'indexed'); % Convert Image to Double Precision

% Convert to double and normalize to the range 0-1, with the brightest

IMG = 1 - rescale(double(projections));
```

5.3 Correction of center of rotation (COR) misalignments

The centre of rotation correction is a very important feature of CT data reconstruction which has not yet been mapped as a standard routine in the ASTRA toolbox. This step is very essential for compensation of some rotation misalignments introduced during the CT data acquisition step. The effects of a misaligned centre of rotation include artefacts such as double edges leading to poor CT data quality. A small difference in subpixel precision can lead to COR misalignments and hence the need to remove this interference through computation of the reconstruction. Figure 5.1 depicts the situation in a perfectly aligned cone-beam geometry setup.

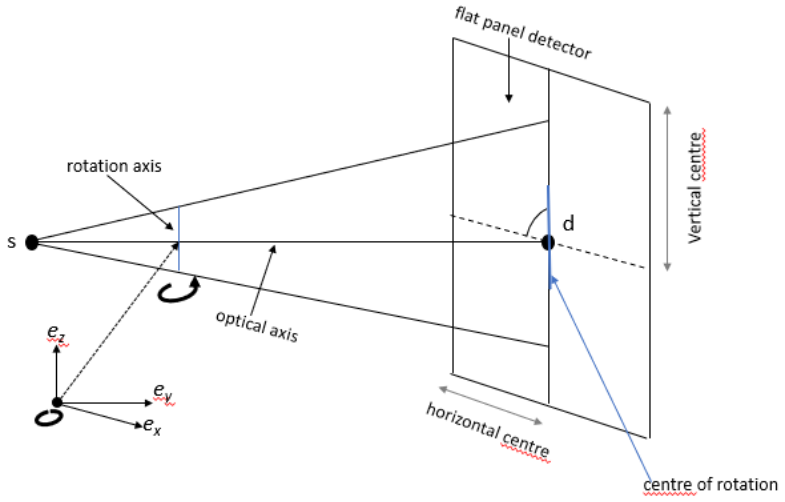

Figure 5.1: An ideal cone-beam scanning experimental setup

The cartesian coordinate system is located on the intersection point of the rotational axis and the optical axis of the CT scanning setup. The optical axis is characterized through the fact that the corresponding x-ray beam hits the flat detector panel surface orthogonally. The projection of the rotation axis onto to the flat panel detector defines the centre of rotation. Furthermore, the specific intersection point which yields the vertical and the horizontal centre coincides with the centre of the detector, a point at which the vector $\boldsymbol{d}$ also points to. The centre of rotation misalignment in our CT scanning setup occurs when the rotational axis is displaced horizontally by amount δu from the optical axis which goes through the origin $\boldsymbol{O}$ of the cartesian coordinate system whilst the x-ray source s and the detector d stay unaffected as shown in figure 5.2.

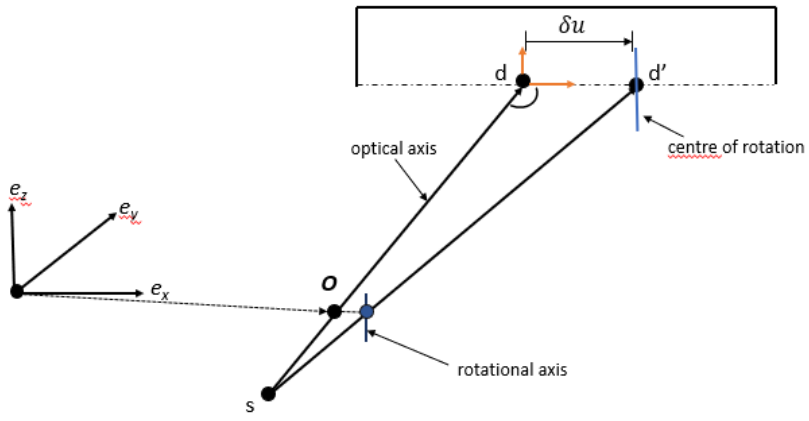

Figure 5.2: COR shift caused by horizontal displacement of the rotational axis from the optical axis.

To correct for these misalignments, we use a COR shift. The vectors {**s, u, v**} remain unmodified and the centre of rotation shift correction is made via the equation

$$\boldsymbol{d}' = \boldsymbol{d} - \delta u\boldsymbol{u} - \delta v\boldsymbol{v}. \qquad (5.9)$$

For given displacements δu and δv, The ASTRA toolbox projection geometry can be corrected through the use of the following code:

```
% correction of COR shift for 3D vectorized cone-beam projection geometry

vectors( : , 4:6) = Vectors( : , 4:6) + . . . δu _Vectors( : , 7:9) + . . .
δv_Vectors( : , 10:12) ;
```

The full code used for this reconstruction will be attached to the appendix of this thesis. However, it should be noted that in our case, the vertical shift δv is zero since the detector and x-ray source are stationary relative to the specimen.

5.4 Conventional cone-beam reconstruction

The reconstruction in this work has been done on the tooth *anteosaurcus magnificus* using a simultaneous iterative reconstruction technique (SIRT) in a MATLAB interface to the ASTRA Toolbox. The Toolbox is added to the MATLAB environment by adding its folder and subfolders to the MATLAB path. The first thing to do is to gather all relevant information about the scan from the Nikon XTH 225 LC instrument that we have used for our experiments. The information is provided in a .xteckt log file.

```
% parameters

distance_source_object = 116 % [mm]

distance_object_detector = 872 % [mm]

detector_pixel_size = 0.2 %[mm]

detector_rows = 2000 % Vertical size of detector [pixels].

detector_cols = 2000 % Horizontal size of detector [pixels].

num_of_projections = 300 % total number of projections is 3000
```

The first step is to determine all the available images. This is done by adding the whole path containing the images to be used in the reconstruction.

```
file = dir('C:\Users\Admin\Documents\CT DATA TOOTH IMAGES\*.tif');
```

The next step is to start a loop to load images into MATLAB. In total 300 projections are used for the reconstruction over a full range [0; 2π]

```
% Start loop to load images into MATLAB
i=0;
proj_num =300;     % number of used projections
step = 3000/proj_num;
```

Preparing space for projections

```
 % Preparing space for projections

% Coordinate order: column (u), angle, row (v)
projections = zeros(810,proj_num,2000);
for i = 1:step:3000
    obr = imread(fullfile('D:\gideon\cropped',file(i).name),'tif').';
    % You need to transpose the projections! Load (rows, columns).
   projections(:,(i+krok-1)/krok,:) = obr;
end
IMG = projections;
```

Converting the image to double precision and normalize to the range 0-1, with the brightest regions corresponding to the thicker parts of the sample.

```
% Convert to double and normalize to the range 0-1, with the brightest regions
corresponding to the thicker parts of the sample.

IMG = 1 - rescale(double(projections));
```

The projection and volume geometries are then defined. Here, a 256× 256× 80 voxel grid is considered. The centre of this volume is located in the central slice, at the axis of rotation. Each projection is recorded as a 2000 × 2000 image with pixel size 0.2 × 0.2mm. The source-to-object and object-to-detector distances are approximately 142 mm and 730mm, respectively. In total, 300 projection images are defined over a full angular range [0; 2π]

```
% Create a 3D volume geometry.
% Parameter order: rows, columns, slices (y, x, z)
% initialized to zero

vol_geom = astra_create_vol_geom(256,256,80);

angles=linspace2(0, 2*pi, proj_num);


proj_geom.DistanceOriginSource = 141.896514892578;
proj_geom.DistanceOriginDetector = 729.603485;
proj_geom.DetectorSpacingX = 0.2;
proj_geom.DetectorSpacingY = 0.2;
VoxelSize =0.0330232521202492;
vectors = zeros(numel(angles), 12);
for i = 1: numel(angles)

% source
      vectors(i,1) = sin(angles(i)) * proj_geom.DistanceOriginSource/VoxelSize;
      vectors(i,2) = -cos(angles(i)) * proj_geom.DistanceOriginSource/VoxelSize;
      vectors(i,3) = 0;

      % center of detector
      vectors(i,4) = -sin(angles(i)) *
proj_geom.DistanceOriginDetector/VoxelSize;
    vectors(i,5) = cos(angles(i)) * proj_geom.DistanceOriginDetector/VoxelSize;
    vectors(i,6) = 0;

      % vector from detector pixel (0,0) to (0,1)
etector pixel (0,0) to (0,1)
      vectors(i,7) = cos(angles(i)) * proj_geom.DetectorSpacingX/VoxelSize;
      vectors(i,8) = sin(angles(i)) * proj_geom.DetectorSpacingX/VoxelSize;
      vectors(i,9) = 0;

      % vector from detector pixel (0,0) to (1,0)
      vectors(i,10) = 0;
      vectors(i,11) = 0;
      vectors(i,12) = proj_geom.DetectorSpacingY/VoxelSize;
end
```

A centre of rotation correction is then done on the projection data before it is subsequently copied into the ASTRA Toolbox memory and space is allocated to store the reconstruction. Each data object is linked to its corresponding geometry object.

```
%Centre of rotation correction.

factor (1) = 1;
factor (2) = 1;
vectors(:,4:6) = vectors(:,4:6) + factor(1) * vectors(:,7:9) + factor(2) *
vectors(:,10:12);

% Parameters: #rows, #columns, vectors
proj_geom = astra_create_proj_geom('cone_vec', 2000, 810, vectors);
rec_id = astra_mex_data3d('create', '-vol', vol_geom);
proj_id = astra_mex_data3d('create', '-proj3d', proj_geom, IMG);
```

As soon as the data is accessible to the toolbox, a reconstruction algorithm can then be configured. In this example, a CUDA accelerated SIRT implementation of 3D data is considered. This configuration gives an identifier referencing the algorithm object. The algorithm identifier is used to perform 50 iterations and the reconstruction data is then retrieved into the MATLAB memory for analysis.

```
% Create reconstruction.
cfg = astra_struct('SIRT3D_CUDA');
cfg.ProjectionDataId = proj_id;
cfg.ReconstructionDataId = rec_id;
alg_id = astra_mex_algorithm('create', cfg);
astra_mex_algorithm('iterate', alg_id, 50);
reconstruction = astra_mex_data3d('get', rec_id);
```

Saving the reconstruction data as 80 tif stack slices.

```
%saving the reconstruction data
for i = 1 : 80
    curIm=uint16(reconstruction(:,:,i));
    curIm=uint16(reconstruction(:,:,i));
    imFilename=strcat('D:\gidz\reconstruction\',sprintf('im%d.tif', i));
    imwrite(curIm,imFilename)
end
```

Cleaning up the ASTRA memory for the next reconstruction.

```
astra_mex_algorithm('delete', alg_id);
astra_mex_data3d('delete', rec_id);
astra_mex_data3d('delete', proj_id);
```

The reconstruction obtained for the tooth is shown in figure 5.3.

(a 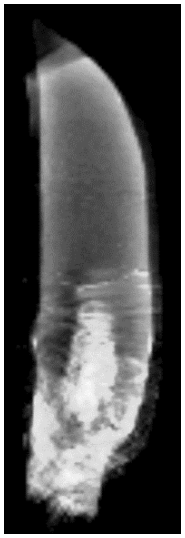 (b)  (c) 

Figure 5.3: (a) A cross-sectional view of the reconstruction of the tooth with the SIRT algorithm in the ASTRA toolbox using 300 projections, (b) A cross-sectional view of the reconstruction of the same specimen with the FBP algorithm in CT Pro 3D using 300 projections, and (c) A cross-sectional view of the reconstruction of the same specimen with the FBP algorithm in CT Pro 3D using 3000 projections.

Another reconstruction was performed using a proximal femur of a *cercppithecoid theropithecus.* The reconstruction was done using the same number of projections and the procedure used for reconstructing the tooth. The results are shown in figure 5.4.

(a) 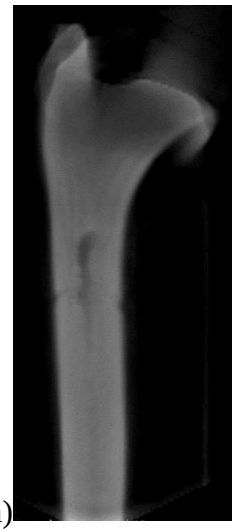 (b)  (c) 

Figure 5.4: (a) A cross-sectional view of the reconstruction of the proximal femur with the SIRT algorithm in the ASTRA toolbox using 300 projections, (b) A cross-sectional view of the reconstruction of the same specimen with the FBP algorithm in CT Pro 3D using 300 projections, and (c) A cross-sectional view of the reconstruction of the same specimen with the FBP algorithm in CT Pro 3D using 3000 projections.

The whole projection data set for the 2 palaeontological specimens used is very large about 23.4 gigabytes. The ASTRA toolbox transmits the sinogram data into an allocated GPU memory in which it is stored for algorithmic operations. Such hardware requirements were not available, and the GPU used has a size of 6 gigabytes. This in turn limits the number of projections that we can currently use for the CT reconstructions using the ASTRA toolbox. We reduced the number of projections to about 300 so that we use only every 10th projection. Due to the computational limitations stated above, the 300 projections used are only about a tenth of the projection data obtained during acquisition. The reconstruction obtained is blurry and noisy due to the use of too large angular steps used to reconstruct the data. Efforts are however underway to acquire a bigger GPU that can accommodate all the projection data in the future. This will in turn allow us to make these iterative algorithms available as a reliable alternative to the FBP.

An analysis of the grey value distribution corresponding to x-ray attenuation was done for the tooth through the use of line profiles measurement tools in ImageJ. This was done to verify the consistency in the shape of the plot corresponding to the intensity values across a slice obtained from the reconstruction data obtained using 300 projections in the ASTRA toolbox in comparison to the data obtained using 3000 projections in CT Pro 3D for a similar slice. The line profiles are drawn passing through similar points in both reconstructions and the results are shown in figure 5.5 and figure 5.6.

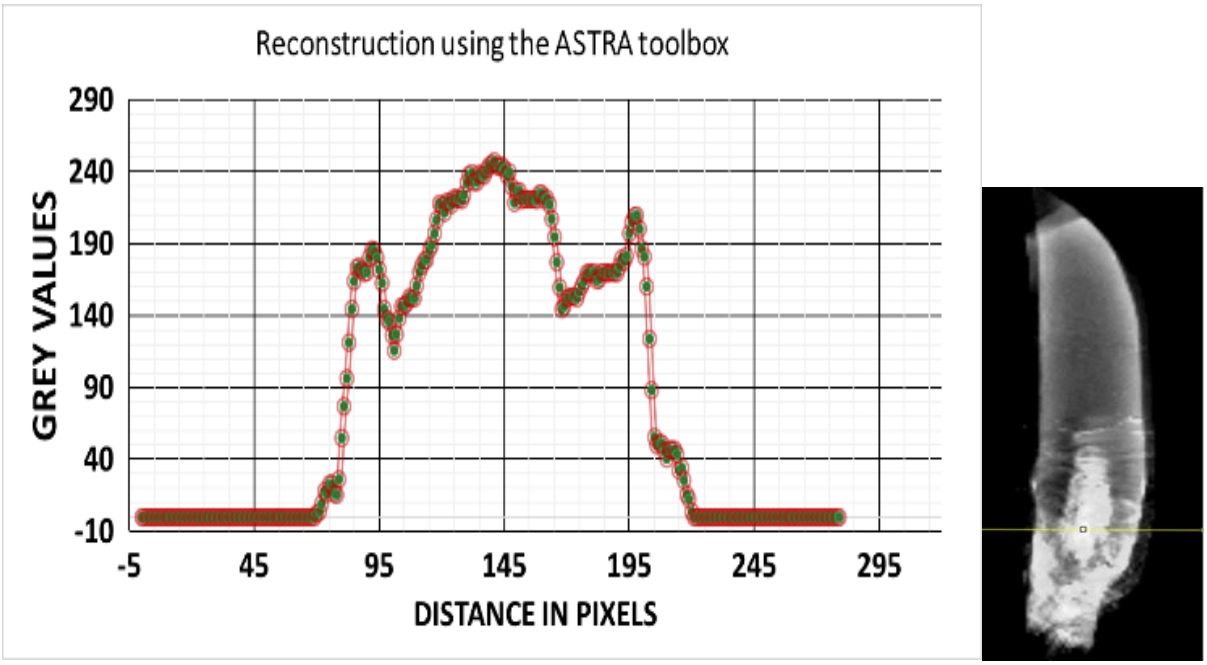

Figure 5.5: A grey value distribution analysis for the tooth reconstructed when reconstructed with the ASTRA toolbox using 300 projections.

Figure 5.6 below shows the grey value distribution of the CT data obtained by reconstructing the tooth with 3000 projections in CT Pro 3D. This was used as a reference point because it was considered to have produced the best image quality in comparison with the other 2 reconstructed datasets.

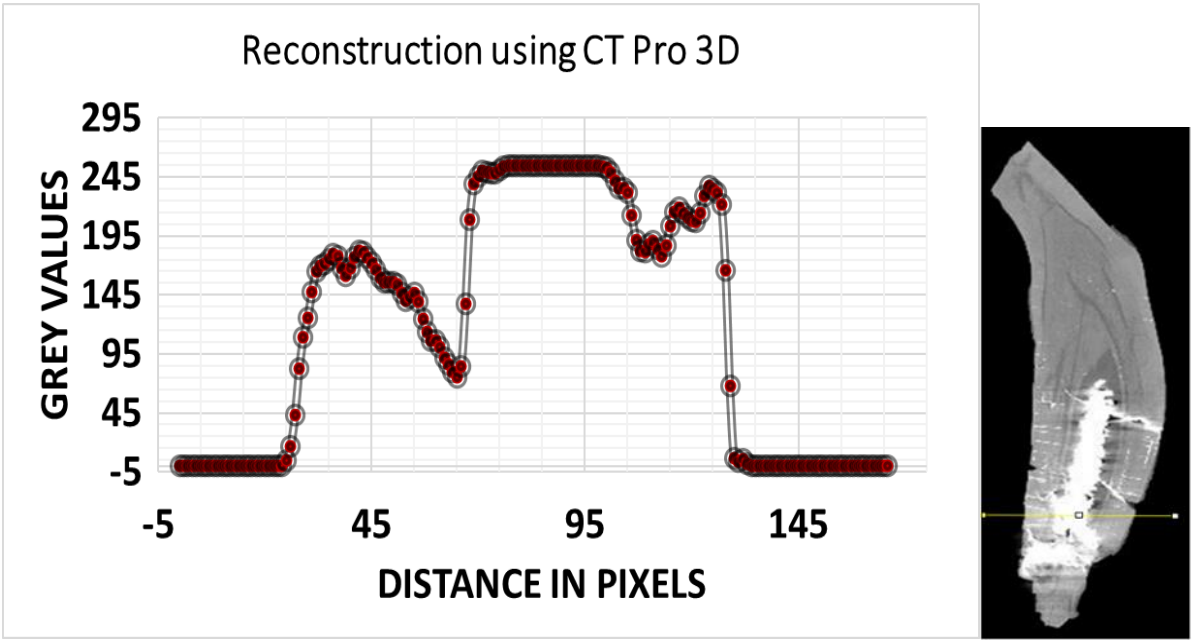

Figure 5.6: A grey value distribution analysis for the tooth reconstructed when reconstructed with CT Pro 3D toolbox using 3000 projections.

The grey value distribution analysis was also done for a femur using the same procedure as above. The results obtained and the results are shown in figure 5.7 and figure 5.8.

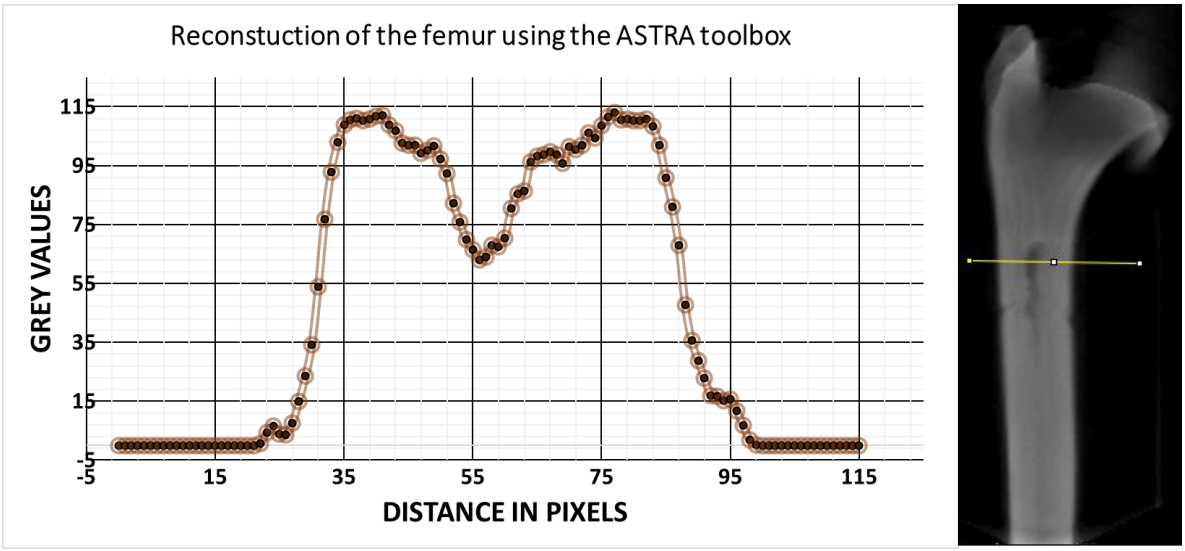

Figure 5.7: A grey value distribution analysis for the femur reconstructed when reconstructed with the ASTRA toolbox using 300 projections.

Figure 5.8 below shows the grey value distribution of the CT data obtained by reconstructing the femur with 3000 projections in CT Pro 3D.

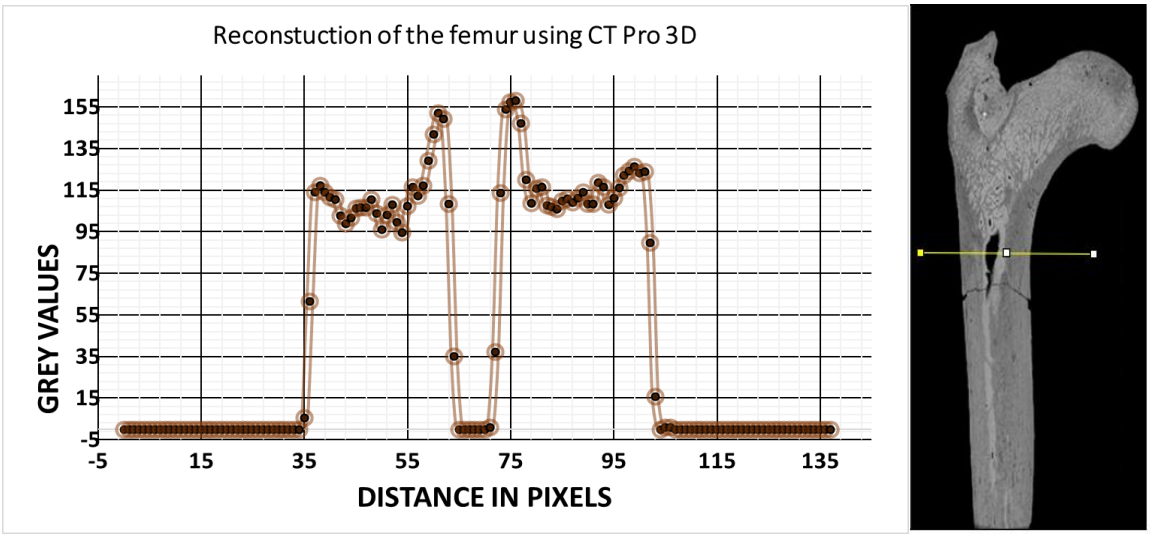

Figure 5.8: A grey value distribution analysis for the femur reconstructed with CT Pro 3D using 3000 projections.

Although we are unable to use a full data set for the reconstruction with the ASTRA toolbox at this stage because of computational limitations, the shape of the intensity profiles obtained from the reconstructed dataset of the tooth in figure 5.5 is the same as the one obtained from

the reconstructed data in figure 5.6 that was used as a reference. In a similar way, the datasets from figures 5.6 and 5.7 follow a similar trend. The comparison between these 2 datasets and their references are a preliminary indication of how efficient the ASTRA toolbox is in the implementation of iterative reconstruction algorithms.

Chapter 6: Concluding remarks

6.1 Introduction

In this report, we have taken two approaches in order to improve computed tomography data quality. Firstly, we have added some image processing steps before reconstructing with the filtered back-projection algorithm. This has been done using the software CT Pro 3D. Then secondly, we have implemented a customizable reconstruction platform, the ASTRA toolbox, and used the SIRT algorithm.

6.2 Image processing before reconstruction

One of the aims of the project mentioned in chapter one was to implement image processing software's to improve CT data quality. This has been fulfilled using the reconstruction software with the filtered back-projection (FBP), which has two distinctive limitations, noise and streak artefacts. ImageJ is a very flexible base for a wide range of image processing applications. The 4 different filters described in chapter 4 were used independently for image enhancement to try and reduce the effect of metallic inclusions on CT image reconstruction. We proposed a histogram-based measure for image quality analysis of computed tomography images. Typically, the scan quality is influenced by beam hardening artefacts and noise. The image measure for the quality Q has been applied on a series of scans obtained by applying the 4 different filters on projections before performing CT reconstructions. The Gaussian filter with a radius of 2 pixels produced the highest image quality due to its ability to reduce noise, streak artefacts, and retain the edges of the images. The median filter with a radius of 2 pixels produced a reconstruction with the lowest image quality as it accentuates noise in the CT data.

From the results obtained in chapter 4, we observe that there is value in using additional image processing steps before reconstruction as there is an improvement in the quality of the data obtained. Figure 4.10 shows that we obtain the best image quality using the Gaussian filter and the median filters. However, this adds an additional challenge as it increases the processing time for reconstructions.

In figure 4.11 the FWHM method was measured for each histogram and used to quantify the image noise as a function of the different filters applied. The Gaussian filter due to its high smoothing ability produced reconstructions with the least noise in comparison to the other filters applied. Implementing the unsharp mask filter accentuates all the high-frequency components

of CT data and hence although it increases edge sharpness it comes with its all shortfalls as in our case it increasing the amount of noise in CT data.

6.3 SIRT reconstruction with the ASTRA toolbox

The reconstruction step is a very essential step in CT as it converts the obtained projection data into interpretable voxel information which is then used to represent the internal structure of the object under investigation.

One of the aims of the project was to make use of the ASTRA toolbox to investigate data reconstruction algorithms from projection images. In this work, we have demonstrated that the ASTRA toolbox is an efficient platform to implement iterative reconstruction algorithms on real-world datasets. The ASTRA toolbox has a plugin that allows the user to specify precisely which geometry they want to use for CT data reconstruction. The prerequisite knowledge with regards to x-ray physics, image reconstruction, and experimental scan setups as well as the mathematical approach to this task is discussed in chapters 2 and 3. Important techniques such as centre of rotation correction and normalization which are used to improve the image quality during reconstruction have been developed using the vectorized version of the projection geometry. There were computational equipment challenges from the projection data size required for reconstruction and the GPU memory. However, meaningful reconstruction were obtained using a tenth of the projection data which was sufficient to demonstrate how the technique works.

The quality of the data obtained using the ASTRA toolbox is higher than what is obtained with the filtered back-projection algorithm for the same number of projections. In chapter 5, figures 5.3 and 5.4, we compared the results of using the SIRT algorithm with using the FBP for 300 projections and it was evident that the quality of data was much better with the former. It is noted that the comparison of SIRT with 300 projections with the FBP using the optimal number of projections of 3000, clearly gives evidence of the need to increase the number of projections used in the iterative case. In the latter case using the filtered back projection algorithm, the features of the sample are well defined, the contrast is improved and the edge determination is superior. This gives an indication that iterative reconstruction algorithms are the future of computed tomography.

Figures 5.7 and 5.8 illustrate the results obtained for reconstructions performed using the ASTRA toolbox with 300 projection and using CT Pro 3D with 3000 projections for a femur.

It can be seen that the features of the femur are well represented but in the SIRT case, however, the image is blurry because of the limited number of projections. The line profiles taken at the same positions clearly show that the edges and features are well determined using more projections as expected. The same analysis applies for figures 5.5 and 5.6 which illustrate the results for the fossilized tooth with high-density inclusions. It is not possible to draw a conclusion on the use of the SIRT algorithm for reducing the effects of metallic inclusions at this point as it is not possible to obtain reconstructions using an optimal number of projections.

6.4 Future work

In this report, we have managed to perform reconstructions using a maximum of 300 projections due to insufficient memory in the GPU. The next steps are to work on parallelizing GPUs in order to distribute the processing so that we can make use of all the projections obtained. Additionally, one could possibly work with the CUDA code in the NVIDIA graphics processing units to try and overcome this hurdle.

The foundation for substantial future work has been set up with the ASTRA toolbox and there are a number of tools that will add and improve the functionality. We will look at implementing beam hardening corrections and filtering methods in the ASTRA toolbox as well as developing data stitching techniques that will be used to combine slice by slice reconstructions. We have already acquired tomography data from the European Synchrotron Radiation Facility (ESRF) for which the coherence of the x-ray beam and the propagation distances allow for phase-contrast imaging. This data will be used to develop phase retrieval capabilities in the ASTRA toolbox and the reconstructions can be compared directly with the data from the ESRF. We will also use gratings to obtain phase contrast in our laboratory-based system and we can add the data treatment capabilities to the customizable toolbox.